AN ANALYSIS OF A NON-CONFORMING HP-DISCONTINUOUS GALERKIN SPECTRAL ELEMENT METHOD FOR WAVE PROPAGATIONS

TAN BUI-THANH [†] AND OMAR GHATTAS [†‡§]

Abstract. We analyze the consistency, stability, and convergence of a hp-discontinuous Galerkin spectral element method. The analysis is simultaneously done for acoustic wave, elastic wave, elastic-acoustic coupling wave and electromagnetic waves. Our analytical results are developed for both conforming and non-conforming approximations on hexahedral meshes using either exact integration using Legendre-Gauss quadratures or inexact integration using Legendre-Gauss-Lobatto quadratures. A mortar-based non-conforming approximation is developed to treat both h and p non-conforming simultaneously. The mortar approach is constructed in such a way that consistency, stability and convergence analyses for conforming approximations go through with minimal modifications, without sacrificing the convergence rates of conforming approximations. In particular, hp-convergence results are proved for non-conforming approximations in the time domain using inexact quadratures.

Key words. Consistency , Stability, Convergence, Discontinuous Galerkin, Non-conforming meshes, Riemann flux, Spectral Element Method, Linear Hyperbolic Equations, Elastic, Acoustic, Electromagnetic, Legendre-Gauss, Legendre-Gauss-Lobatto.

AMS subject classifications. 15A15, 15A09, 15A23

1. Introduction. The Discontinuous Galerkin (DG) method which was originally developed by Reed and Hill [26] for the neutron transport equation has been extended to other types of partial differential equations (PDEs) [9]. In particular, it emerges as one of the best methods for hyperbolic PDEs [8, 10]. Among its many advantages over the classical finite volume and finite element methods, it has the ability to treat solution with high gradient such as shock waves, provides the flexibility to deal with complex geometries, and it is highly parallelizable due to its compact stencil. The best advantage is probably its ability for hp adaptation in a natural manner [5]. This makes the DG method as the most promising approach for large-scale computation with high accuracy [33]. The question on how to treat non-conforming interfaces between elements due to both local p-refinement and local h-refinement can be resolved in many ways. A highly parallelizable non-conforming treatment can be found in Kopriva [18, 22]. This method replaces a non-conforming face by mortars that connect pairs of contributing elements. The actual computations are performed on the mortars instead on the non-conforming face, and the results are then projected on the contributing element faces. Since the mortar approach of Kopriva has the same compact stencil of the DG method, it makes the adaptivity highly parallelizable [33], while numerically preserving the stability and the optimal order convergence [22, 33]. Since then, there has been no attempts to theoretically study the stability and the convergence of the mortar-based non-conforming approximation of Kopriva.

The famous classical Lax-Richtmyer equivalence theorem [24] has far reaching consequences in numerical analysis. The theorem is so important that it is sometimes called the fundamental theorem of numerical analysis. One side of the theorem, which is widely used in practice, says that for well-posed linear differential problems,

[†]Institute for Computational Engineering & Sciences, The University of Texas at Austin, Austin, TX 78712, USA.

[‡]Jackson School of Geosciences, The University of Texas at Austin, Austin, TX 78712, USA.

[§]Department of Mechanical Engineering, The University of Texas at Austin, Austin, TX 78712, USA.

consistency and stability of a difference method imply its convergence. Consistency is typically easy to verify while a direct proof of convergence is difficult due to the fact that knowledge about the exact solution is required. The stability, on the other hand, is purely a property of the difference approximation and hence in principle can be controlled by devising a numerical approximation fulfilling the stability. The Lax-Richtmyer equivalence theorem, as an alternative in proving convergence of a numerical method, says that consistency and stability are all we need for the convergence. Nevertheless, there are areas in which the equivalence theorem may not be needed since one can prove convergence directly and easily, e.g. numerical differentiation [17]. Moreover, typical applications of the Lax-Richtmyer theorem provide an error upper bound that grows exponentially in time. In practice, it is observed that the error grows with much lower rate. In particular, it has been shown that a direct proof of convergence is possible and the error grows at most linearly in time for a class of discontinuous Galerkin methods [13, 14].

In this paper, we theoretically study the consistency, stability, and convergence of a discontinuous Galerkin Spectral element method (DGSEM). In particular, we present the stability proof using the energy method for the DGSEM with the mortar-based non-conforming approximation of Kopriva [18, 22]. We anticipate that the results of our study can be applied to a large class of linear conservation laws. However, to be concrete, the proof is simultaneously done for elastic, acoustic, elastic–acoustic coupling wave equations and electromagnetic wave equations as examples for conservation laws governed by linear hyperbolic partial differential equations. Instead of discretizing the mortars with exact numerical quadratures as in [22, 33], which we are not able to prove stability for the interesting case of Legendre-Gauss-Lobatto quadrature, we propose to discretize them using a special quadrature rule which facilitates the stability proof. We manage to prove the stability and convergence for both exact numerical quadrature using the Legendre-Gauss rule and inexact numerical quadrature using the Legendre-Gauss-Lobatto rule. For the inexact numerical integration, we use the tensor product quadrature rule as it allows us to perform discrete integration by parts [29, 21], which in turns paves the way for the stability and convergence proofs.

The Riemann numerical flux is our main ingredient in proving the stability and convergence. As the PDEs in this paper are linear, the exact Riemann flux is possible [30], hence it is used in our proofs. As will be shown, it is the dissipative nature of the Riemann flux that makes the DGSEM stable. Therefore we anticipate that our results also hold for other dissipative fluxes such as the stabilized Lax-Friedrichs numerical flux [27].

We mostly restrict ourselves to the cases of affine hexahedral meshes in which we detail the derivations and the proofs. In order to make the proofs concrete, three-dimensional elastic–acoustic and electromagnetic waves are used as examples. Of course, all the results hold for two-dimensional problems as well.

The paper is organized as follows. Section 2 briefly describes a weak setting for general linear conservation laws. Section 3 presents a *hp* DGSEM for both elastic-acoustic and electromagnetic waves. We then prove the stability for conforming meshes in Section 4. The detailed description of our mortar-based non-conforming approximation is given in Section 5 which is followed by the non-conforming stability proof in Section 6. The direct proof of convergence is carried out in Section 7, and extensive numerical results supporting our analytical findings are presented in Section 8. Finally, Section 9 concludes our paper.

2. General setting for linear hyperbolic conservation laws. We are interested in linear wave equations governed by linear hyperbolic conservation laws. In the strong form, a general equation is given as

$$\mathcal{Q}\frac{\partial \mathfrak{q}}{\partial t} + \nabla_{\boldsymbol{x}} \cdot (\mathfrak{F}\mathfrak{q}) = \mathfrak{g}, \quad \mathfrak{q} \in \mathcal{V}, \boldsymbol{x} \in \mathcal{D},$$

with $\mathcal{V}$ as the solution space, to be specified later, over the domain of interest $\mathcal{D}$, and with appropriate initial and boundary conditions. The subscript $\boldsymbol{x}$ denotes the $\boldsymbol{x}$-coordinate system in which the divergence operator acts. Next, multiplying by the test function $\mathfrak{p}$, the corresponding weak formulation is obtained as

$$\int_{\mathcal{D}} \mathcal{Q}\frac{\partial \mathfrak{q}}{\partial t} \cdot \mathfrak{p}\, d\boldsymbol{x} + \int_{\mathcal{D}} \nabla_{\boldsymbol{x}} \cdot (\mathfrak{F}\mathfrak{q}) \cdot \mathfrak{p}\, d\boldsymbol{x} = \int_{\mathcal{D}} \mathfrak{g} \cdot \mathfrak{p}\, d\boldsymbol{x},$$

where "$\cdot$" denotes the Euclidean inner product.

We next partition the domain $\mathcal{D}$ into N_{el} non-overlapping hexahedral elements such that $\mathcal{D} = \bigcup_{e=1}^{N_{\text{el}}} \mathsf{D}^e$, and integrate the weak formulation by parts twice to obtain

$$\begin{aligned}
&\sum_e \int_{\mathsf{D}^e} \mathcal{Q}^e \frac{\partial \mathfrak{q}^e}{\partial t} \cdot \mathfrak{p}^e\, d\boldsymbol{x} + \sum_e \int_{\mathsf{D}^e} \nabla_{\boldsymbol{x}} \cdot (\mathfrak{F}\mathfrak{q}^e) \cdot \mathfrak{p}^e\, d\boldsymbol{x} \\
&+ \sum_e \int_{\partial \mathsf{D}^e} \boldsymbol{n} \cdot \left[(\mathfrak{F}\mathfrak{q}^e)^* - \mathfrak{F}\mathfrak{q}^e \right] \cdot \mathfrak{p}^e\, d\boldsymbol{x} = \sum_e \int_{\mathsf{D}^e} \mathfrak{g}^e \cdot \mathfrak{p}^e\, d\boldsymbol{x},
\end{aligned} \tag{2.1}$$

where a consistent numerical flux $(\mathfrak{F}\mathfrak{q}^e)^*$ has been introduced to couple solutions of neighboring elements, and $(\cdot)^e$ denotes the restriction on the e-th element of the corresponding quantity.

Equation (2.1) is known as the strong form in the context of nodal discontinuous Galerkin methods [14]. For the DGSEM described in this paper, the strong form (integrating the flux terms by parts twice) and the weak form (integrating the flux terms by parts once) are equivalent [29, 21], and hence all the results in the paper hold for the weak form as well.

3. A discontinuous Galerkin spectral element method. In this section, we briefly describe an *hp*-discontinuous Galerkin spectral element method. We approximate each element D^e by polynomials, again denoted by D^e, such that each element D^e is mapped to the reference hexahedron $\hat{\mathsf{D}} = [-1, 1]^3$ by a C^1-diffeomorphism $\boldsymbol{X}^e$, and $\mathcal{D} \approx \mathcal{D}^{N_{el}} = \bigcup_{e=1}^{N_{el}} \mathsf{D}^e$. Equation (2.1) can be written in terms of $\hat{\mathsf{D}}$ as

$$\begin{aligned}
&\sum_e \int_{\hat{\mathsf{D}}} J^e \mathcal{Q}^e \frac{\partial \mathfrak{q}^e}{\partial t} \cdot \mathfrak{p}^e\, d\boldsymbol{r} + \sum_e \int_{\hat{\mathsf{D}}} \nabla_{\boldsymbol{r}} \cdot \left(\tilde{\mathfrak{F}}\mathfrak{q}^e \right) \cdot \mathfrak{p}^e\, d\boldsymbol{r} \\
&+ \sum_e \int_{\partial \hat{\mathsf{D}}} \tilde{\boldsymbol{n}} \cdot \left[\left(\tilde{\mathfrak{F}}\mathfrak{q}^e \right)^* - \tilde{\mathfrak{F}}\mathfrak{q}^e \right] \cdot \mathfrak{p}^e\, d\boldsymbol{r} = \sum_e \int_{\hat{\mathsf{D}}} J^e \mathfrak{g}^e \cdot \mathfrak{p}^e\, d\boldsymbol{r},
\end{aligned} \tag{3.1}$$

where $\boldsymbol{r} = (r_1, r_2, r_3) \in \hat{\mathsf{D}}$ represents the reference coordinates and J^e is the Jacobian of the transformation. The outward normal on the boundary of the master element $\hat{\mathsf{D}}$ is denoted by $\tilde{\boldsymbol{n}}$, and the contravariant flux [19] is defined as

$$\tilde{\mathfrak{F}}^i = J^e \boldsymbol{a}^i \cdot \mathfrak{F}, \quad i = 1, 2, 3,$$

with $\boldsymbol{a}^i$ as the contravariant basis vectors.

We now describe the approximation spaces for wave propagation in elastic, acoustic, and coupled elastic–acoustic media using the strain–velocity formulation, and for Maxwell's equations for electromagnetic wave propagation. Equation (3.1) can be specialized to the elastic–acoustic wave propagation case by the following definitions,

$$\mathfrak{q} = \begin{pmatrix} \boldsymbol{E} \\ \boldsymbol{v} \end{pmatrix} \in \mathcal{V}, \qquad \mathcal{Q} = \begin{pmatrix} \mathsf{I} & \mathbf{0} \\ \mathbf{0} & \rho \boldsymbol{I} \end{pmatrix}, \qquad \mathfrak{g} = \begin{pmatrix} \mathbf{0} \\ \boldsymbol{f} \end{pmatrix} \in \mathcal{V},$$

with I denoting the fourth-order identity tensor, $\mathbf{0}$ the zero tensors of appropriate sizes, $\boldsymbol{I}$ the second-order identity tensor, $\boldsymbol{E}$ the strain tensor, $\boldsymbol{v}$ the velocity vector, $\boldsymbol{f}$ the external volumetric forces, and ρ the density.

The action of the flux operator $\mathfrak{F}$ on the strain–velocity unknowns $\mathfrak{q}$ can be shown to be [33]

$$(\mathfrak{F}\mathfrak{q})_i = \begin{pmatrix} -\frac{1}{2}\left(\boldsymbol{v} \otimes \boldsymbol{e}_i + \boldsymbol{e}_i \otimes \boldsymbol{v}\right) \\ -\left(\mathsf{C}\boldsymbol{E}\right)\boldsymbol{e}_i \end{pmatrix} \in \mathcal{V} \quad \text{for } i = 1, 2, 3.$$

For isotropic linear elasticity, the strain tensor $\boldsymbol{E}$ and the Cauchy stress tensor $\boldsymbol{S}$ are related by the fourth-order constitutive tensor C,

$$\boldsymbol{S} = \mathsf{C}\boldsymbol{E},$$

with $S = \lambda \operatorname{tr}(\boldsymbol{E})\boldsymbol{I} + 2\mu\boldsymbol{E}$, where λ and μ are the two Lamé constants characterizing the isotropic constitutive relationship. The longitudinal wave speed c_p and shear wave speed c_s are defined in terms of the Lamé constants and density by

$$c_p = \sqrt{\frac{\lambda + 2\mu}{\rho}} \qquad \text{and} \qquad c_s = \sqrt{\frac{\mu}{\rho}},$$

with $c_s = 0$ in acoustic regions by virtue of $\mu = 0$.

As in [33], we choose the solution space to be $\mathcal{V} = \boldsymbol{V}^{3\times 3}_{\text{sym}} \oplus \boldsymbol{V}^3$, where $\boldsymbol{V}$ denotes a space of sufficiently smooth functions defined on $\mathcal{D}$ so that (2.1) makes sense. The discontinuous approximation to $\boldsymbol{V}$ is given by

$$\boldsymbol{V}_d := \{q_d \in L^2(\mathcal{D}^{N_{\text{el}}}) : q_d|_{\mathsf{D}^e} \circ \boldsymbol{X}^e \in \mathbb{Q}_{N_e}(\hat{\mathsf{D}})\},$$

where $\mathbb{Q}_{N_e}$ is the tensor product of one-dimensional polynomials of degree at most N_e on the reference element. It should be pointed out that the polynomial orders need not be the same for all directions, but for clarity, we use the same order in all directions. The numerical solution $\mathfrak{q}_d \in \boldsymbol{V}^{3\times 3}_{d,\text{sym}} \oplus \boldsymbol{V}^3_d$ of the elastic-acoustic coupling restricted on each element D^e is specified as

$$\mathfrak{q}_d|_{\mathsf{D}^e} \circ \boldsymbol{X}^e \in \mathcal{V}^e_d \equiv \mathbb{Q}^{3\times 3}_{N_e,\text{sym}} \oplus \mathbb{Q}^3_{N_e}, \qquad \boldsymbol{X}^e : \hat{\mathsf{D}} \to \mathsf{D}^e.$$

Before introducing the Riemann flux, let us recall the following standard DG notation for quantities associated with element interfaces:

$$[\![\mathfrak{q}]\!] = \mathfrak{q}^+ \cdot \boldsymbol{n}^+ + \mathfrak{q}^- \cdot \boldsymbol{n}^-, \quad [\mathfrak{q}] = \mathfrak{q}^- - \mathfrak{q}^+, \quad \{\{Z\}\} = \frac{Z^+ + Z^-}{2},$$

where the positive and negative signs indicate element interior and exterior, respectively.

For linear conservation laws one can solve the Riemann problem exactly by various methods [30]. Using the Rankine–Hugoniot approach, Wilcox *et al.* [33] show that the exact Riemann flux for the strain equation is given by

$$\begin{aligned}\boldsymbol{n}\cdot\left[(\mathfrak{F}\mathfrak{q})^*_{\boldsymbol{E}}-(\mathfrak{F}\mathfrak{q})_{\boldsymbol{E}}\right] &= \left(k_0\boldsymbol{n}\cdot[\![\mathbf{C}\boldsymbol{E}]\!]+k_0\rho^+c_p^+\,[\![\boldsymbol{v}]\!]\right)\boldsymbol{n}\otimes\boldsymbol{n}\\ &\quad -k_1\,\mathrm{sym}\left(\boldsymbol{n}\otimes(\boldsymbol{n}\times(\boldsymbol{n}\times[\![\mathbf{C}\boldsymbol{E}]\!]))\right)\\ &\quad -k_1\rho^+c_s^+\,\mathrm{sym}\left(\boldsymbol{n}\otimes(\boldsymbol{n}\times(\boldsymbol{n}\times[\boldsymbol{v}]))\right),\end{aligned}$$

and for the velocity equation by

$$\begin{aligned}\boldsymbol{n}\cdot\left[(\mathfrak{F}\mathfrak{q})^*_{\boldsymbol{v}}-(\mathfrak{F}\mathfrak{q})_{\boldsymbol{v}}\right] &= \left(k_0\boldsymbol{n}\cdot[\![\mathbf{C}\boldsymbol{E}]\!]+k_0\rho^+c_p^+\,[\![\boldsymbol{v}]\!]\right)\rho^-c_p^-\boldsymbol{n}\\ &\quad -k_1\rho^-c_s^-\boldsymbol{n}\times(\boldsymbol{n}\times[\![\mathbf{C}\boldsymbol{E}]\!])\\ &\quad -k_1\rho^+c_s^+\rho^-c_s^-\boldsymbol{n}\times(\boldsymbol{n}\times[\boldsymbol{v}]),\end{aligned}$$

where

$$k_0=\frac{1}{\rho^-c_p^-+\rho^+c_p^+}.$$

For elastic–elastic and elastic–acoustic interfaces, with an elastic medium on the inward side (i.e., $\mu^-\neq 0$),

$$k_1=\frac{1}{\rho^-c_s^-+\rho^+c_s^+}.$$

With an acoustic medium on the inward side, $\mu^-=0$, we simply take

$$k_1=0.$$

Here, we will consider only traction boundary conditions $\boldsymbol{S}\boldsymbol{n}=\boldsymbol{t}_{bc}$, where $\boldsymbol{t}_{bc}$ is the prescribed traction. The traction condition is enforced by the following mirror principle,

$$\begin{aligned}[\![\boldsymbol{v}]\!]&=[\boldsymbol{v}]=\mathbf{0},\\ [\![\boldsymbol{S}]\!]&=-2\left(\boldsymbol{t}_{bc}-\boldsymbol{S}^-\boldsymbol{n}\right),\end{aligned}$$

which applies to both elastic or acoustic media.

We next specialize (3.1) to the case of Maxwell's equations. In this case,

$$\mathfrak{q}=\begin{pmatrix}\boldsymbol{E}\\ \boldsymbol{H}\end{pmatrix}\in\mathcal{V},\qquad \mathcal{Q}=\begin{pmatrix}\varepsilon\boldsymbol{I} & \mathbf{0}\\ \mathbf{0} & \mu\boldsymbol{I}\end{pmatrix},\qquad \mathfrak{g}=\begin{pmatrix}\mathbf{0}\\ \mathbf{0}\end{pmatrix}\in\mathcal{V},$$

where $\boldsymbol{E}$ denotes the electric field, $\boldsymbol{H}$ the magnetic field, μ the permeability, and ε the permittivity.

The action of the flux operator $\mathfrak{F}$ on the electromagnetic field $\mathfrak{q}$ is defined by

$$(\mathfrak{F}\mathfrak{q})_i=\begin{pmatrix}-\boldsymbol{e}_i\times\boldsymbol{H}\\ \boldsymbol{e}_i\times\boldsymbol{E}\end{pmatrix}\in\mathcal{V}\quad\text{for } i=1,2,3,$$

where $\mathcal{V} = \boldsymbol{V}^3$ and

$$\mathfrak{q}_d|_{\mathsf{D}^e} \circ \boldsymbol{X}^e \in \mathcal{V}_d^e \equiv \mathbb{Q}_{N_e}^3.$$

The exact Riemann numerical flux for electric equation can be shown to be [14]

$$\boldsymbol{n} \cdot \left[(\mathfrak{Fq})^*_{\boldsymbol{E}} - (\mathfrak{Fq})_{\boldsymbol{E}} \right] = \frac{1}{2\left\{\{Z\}\right\}} \boldsymbol{n} \times \left(Z^+ [\boldsymbol{H}] - \boldsymbol{n} \times [\boldsymbol{E}] \right),$$

and for the magnetic equation,

$$\boldsymbol{n} \cdot \left[(\mathfrak{Fq})^*_{\boldsymbol{H}} - (\mathfrak{Fq})_{\boldsymbol{H}} \right] = -\frac{1}{2\left\{\{Y\}\right\}} \boldsymbol{n} \times \left(Y^+ [\boldsymbol{E}] + \boldsymbol{n} \times [\boldsymbol{H}] \right),$$

where

$$Z^{\pm} = \frac{1}{Y^{\pm}} = \sqrt{\frac{\mu^{\pm}}{\epsilon^{\pm}}}.$$

Similar to the elastic–acoustic coupling case, we use the mirror principle to enforce a perfect electric conductor (PEC) boundary condition by

$$\begin{aligned} Z^- = Z^+, \quad Y^- = Y^+, \\ \boldsymbol{n} \times [\boldsymbol{H}] = 0, \\ \boldsymbol{n} \times [\boldsymbol{E}] = 2\boldsymbol{n} \times \boldsymbol{E}^- \end{aligned}$$

and a perfect magnetic conductor (PMC) boundary condition by

$$\begin{aligned} Z^- = Z^+, \quad Y^- = Y^+, \\ \boldsymbol{n} \times [\boldsymbol{E}] = 0, \\ \boldsymbol{n} \times [\boldsymbol{H}] = 2\boldsymbol{n} \times \boldsymbol{H}^-. \end{aligned}$$

For dielectric boundary conditions we use

$$\boldsymbol{n} \times \boldsymbol{E}^- = \boldsymbol{n} \times \boldsymbol{E}^+, \quad \boldsymbol{n} \times \boldsymbol{H}^- = \boldsymbol{n} \times \boldsymbol{H}^+.$$

In order to unify the treatment for elastic, acoustic, coupled elastic–acoustic, and electromagnetic waves, we define a generic polynomial space $\mathcal{P}_N$ whose meaning will be clear in each context. For example, if we write $\mathfrak{q}^e \in \mathcal{P}_N$, this identifies $\mathcal{P}_N \equiv \mathcal{V}_d^e$.

The tensor product basis for $\mathbb{Q}_N$ is built upon the following one-dimensional Lagrange basis

$$\ell_l(\xi) = \prod_{\substack{k=0,1,\ldots,N \\ k \neq l}} \frac{\xi - \xi_k}{\xi_l - \xi_k},$$

where the Nth-degree Legendre-Gauss-Lobatto (LGL) points, or Nth-degree Legendre-Gauss points (LG), $\{\xi_l\}$ on $[-1, 1]$ for $l = 0, \ldots, N$, are chosen as both the interpolation and quadrature points. This is also known as the collocation approach. The Lagrange interpolant of a function $f(\boldsymbol{r})$ on the reference element $\hat{\mathsf{D}}$ is defined through the interpolation operator $\mathcal{I}_N$ as

$$\mathcal{I}_N(f) = \sum_{l,m,n=0}^{N} f_{lmn} \ell_l(r_1) \ell_m(r_2) \ell_n(r_3),$$

where

$$f_{lmn} = f\left(\boldsymbol{\xi}_{lmn}\right), \qquad \boldsymbol{\xi}_{lmn} = \left(\xi_l, \xi_m, \xi_n\right) \in \hat{\mathsf{D}}.$$

A typical collocation approach [20] in semi-discretizing (3.1) is as follows. Find $\mathfrak{q} \in \mathcal{V}_d$ such that

$$\begin{aligned}
&\sum_e \int_{\hat{\mathsf{D}}} \mathcal{I}_{N_e}\left(\mathcal{I}_{N_e}\left(J^e\right)\mathcal{I}_{N_e}\left(\mathcal{Q}^e\right)\frac{\partial \mathfrak{q}^e}{\partial t}\right)\cdot \mathfrak{p}^e\, d\boldsymbol{r} + \sum_e \int_{\hat{\mathsf{D}}} \nabla_{\boldsymbol{r}}\cdot \mathcal{I}_{N_e}\left(\tilde{\mathfrak{F}}\mathfrak{q}^e\right)\cdot \mathfrak{p}^e\, d\boldsymbol{r} \\
&+ \sum_e \int_{\partial\hat{\mathsf{D}}} \tilde{\boldsymbol{n}}\cdot\left[\mathcal{I}_{N_e}\left(\left(\tilde{\mathfrak{F}}\mathfrak{q}^e\right)^*\right) - \mathcal{I}_{N_e}\left(\tilde{\mathfrak{F}}\mathfrak{q}^e\right)\right]\cdot \mathfrak{p}^e\, d\boldsymbol{r} \\
&= \sum_e \int_{\hat{\mathsf{D}}} \mathcal{I}_{N_e}\left(\mathcal{I}_{N_e}\left(J^e\right)\mathcal{I}_{N_e}\left(\mathfrak{g}^e\right)\right)\cdot \mathfrak{p}^e\, d\boldsymbol{r}, \quad \forall \mathfrak{p} \in \mathcal{V}_d,
\end{aligned}$$

where

$$\mathcal{I}_{N_e}\left(\tilde{\mathfrak{F}}^i\right) = \mathcal{I}_{N_e}\left(\mathcal{I}_{N_e}\left(J^e\boldsymbol{a}^i\right)\cdot\mathcal{I}_{N_e}\left(\mathfrak{F}\right)\right).$$

The direct consequence of the above collocation is that the integrand in each integral is at most of order $2N_e$ in each direction $r_i, i = 1, 2, 3$. Numerical quadrature yields the following semi-discrete form,

$$\begin{aligned}
&\sum_e \int_{\hat{\mathsf{D}},N_e} \mathcal{I}_{N_e}\left(\mathcal{I}_{N_e}\left(J^e\right)\mathcal{I}_{N_e}\left(\mathcal{Q}^e\right)\frac{\partial \mathfrak{q}^e}{\partial t}\right)\cdot \mathfrak{p}^e\, d\boldsymbol{r} + \sum_e \int_{\hat{\mathsf{D}},N_e} \nabla_{\boldsymbol{r}}\cdot \mathcal{I}_{N_e}\left(\tilde{\mathfrak{F}}\mathfrak{q}^e\right)\cdot \mathfrak{p}^e\, d\boldsymbol{r} \\
&+ \sum_e \int_{\partial\hat{\mathsf{D}},N_e} \tilde{\boldsymbol{n}}\cdot\left[\mathcal{I}_{N_e}\left(\left(\tilde{\mathfrak{F}}\mathfrak{q}^e\right)^*\right) - \mathcal{I}_{N_e}\left(\tilde{\mathfrak{F}}\mathfrak{q}^e\right)\right]\cdot \mathfrak{p}^e\, d\boldsymbol{r} \\
&= \sum_e \int_{\hat{\mathsf{D}},N_e} \mathcal{I}_{N_e}\left(\mathcal{I}_{N_e}\left(J^e\right)\mathcal{I}_{N_e}\left(\mathfrak{g}^e\right)\right)\cdot \mathfrak{p}^e\, d\boldsymbol{r}, \quad \forall \mathfrak{p} \in \mathcal{V}_d,
\end{aligned} \tag{3.2}$$

where the subscript N_e in the integrals means that the integrals are numerically evaluated using the corresponding N_eth-degree LGL (or LG) quadrature rule.

4. Semi-discrete stability for conforming meshes. In this section, we provide a stability proof for the both elastic–acoustic and electromagnetic cases on conforming meshes. By conforming meshes we mean that the intersection of two elements is either an entire face, and entire edge, or a corner, and that the solution order is the same for all elements. It is sufficient to prove semi-discrete stability since, by a result in [23] (and the references therein), if the semi-discrete equation is stable, the fully discrete system with the time derivative discretized by a locally stable Runge-Kutta (for example the classical 4th-order Runge-Kutta method) is stable as well, as long as the time step is sufficiently small.

Here, we employ the energy approach to prove stability. For the elastic–acoustic case, the semi-discrete energy functional $\mathcal{E}_d(t)$ is defined as

$$\mathcal{E}_d(t) := \sum_{e=1}^{N_{\text{el}}} \mathcal{E}^e_{N^e}(t) \quad \text{where} \quad \mathcal{E}^e_{N^e}(t) := \frac{1}{2}\int_{\mathsf{D}^e,N_e} \left(\boldsymbol{E} : (\mathbf{C}\boldsymbol{E}) + \rho\boldsymbol{v}\cdot\boldsymbol{v}\right) d\boldsymbol{x},$$

and for the electromagnetic case as

$$\mathcal{E}_d(t) := \sum_{e=1}^{N_{\text{el}}} \mathcal{E}^e_{N^e}(t) \quad \text{where} \quad \mathcal{E}^e_{N^e}(t) := \frac{1}{2}\int_{\mathsf{D}^e,N_e} \left(\epsilon\boldsymbol{E}\cdot\boldsymbol{E} + \mu\boldsymbol{H}\cdot\boldsymbol{H}\right) d\boldsymbol{x}.$$

For convenience, we define the element-wise discrete L^2 inner product and the induced norm on a generic domain D, which could be an element or its boundary, as

$$(\mathfrak{q},\mathfrak{p})_{D,N} = \int_{D,N} \mathfrak{q}\cdot\mathfrak{p}\, d\boldsymbol{x}, \quad \|\mathfrak{q}\|^2_{D,N} = \int_{D,N} \mathfrak{q}\cdot\mathfrak{q}\, d\boldsymbol{x},$$

and their continuous counterparts as

$$(\mathfrak{q},\mathfrak{p})_{D} = \int_{D} \mathfrak{q}\cdot\mathfrak{p}\, d\boldsymbol{x}, \quad \|\mathfrak{q}\|^2_{D} = \int_{D} \mathfrak{q}\cdot\mathfrak{p}\, d\boldsymbol{x}.$$

The discrete global L^2 norm is computed as the summation of the element-wise contributions

$$\|\mathfrak{q}\|^2_{\mathcal{D}^{N_{\text{el}}},d} = \sum_e \|\mathfrak{q}\|^2_{\mathsf{D}^e,N^e}.$$

THEOREM 1. *Assume the mesh is affine and conforming with solution order N, then the DGSEM discretization is stable in the following sense:*

$$\frac{d}{dt}\mathcal{E}_d \le \frac{1}{2}\left(\mathcal{E}_d + \|\mathcal{I}_N\mathfrak{g}\|^2_{\mathcal{D}^{N_{el}},d}\right).$$

Moreover, if $\mathfrak{g}=0$, then $\frac{d}{dt}\mathcal{E}_d \le 0$.

Proof. Substituting $\mathfrak{p} := \begin{pmatrix}\boldsymbol{S}\\ \boldsymbol{v}\end{pmatrix} := \begin{pmatrix}\mathbf{C}\boldsymbol{E}\\ \boldsymbol{v}\end{pmatrix}$ for the elastic–acoustic coupling case, and $\mathfrak{p}=\mathfrak{q}$ for the electromagnetic case, into (3.2), and using a discrete integration by parts formula [29, 21], we obtain

$$\begin{aligned}\sum_e \frac{d}{dt}\mathcal{E}^e_d = \frac{1}{2}\sum_e \int_{\hat{\mathsf{D}},N}\left[\mathcal{I}_N\left(\tilde{\mathfrak{F}}\mathfrak{q}^e\right)\cdot\nabla_{\boldsymbol{r}}\cdot\mathfrak{p}^e - \nabla_{\boldsymbol{r}}\cdot\mathcal{I}_N\left(\tilde{\mathfrak{F}}\mathfrak{q}^e\right)\cdot\mathfrak{p}^e\right] d\boldsymbol{r}\\ + \sum_e -\int_{\partial\hat{\mathsf{D}},N}\tilde{\boldsymbol{n}}\cdot\left[\left(\tilde{\mathfrak{F}}\mathfrak{q}^e\right)^* - \frac{1}{2}\tilde{\mathfrak{F}}\mathfrak{q}^e\right]\cdot\mathfrak{p}^e\, d\boldsymbol{r} + \sum_e\int_{\hat{\mathsf{D}},N} J^e\mathfrak{g}^e\cdot\mathfrak{p}^e\, d\boldsymbol{r}, \quad (4.1)\end{aligned}$$

where we have dropped the interpolation operator $\mathcal{I}_{N_e}$ in the last two terms on the right side of (4.1) since the interpolation is an orthogonal projection with the discrete L^2 inner product [7], e.g.,

$$\int_{D,N} qp\, d\boldsymbol{x} = \int_{D,N}\mathcal{I}_N(q)\, p\, d\boldsymbol{x}.$$

For affine meshes, the metric terms $J^e\boldsymbol{a}^i, i=1,2,3$ are constant, and thus

$$\mathcal{I}_N\left(\tilde{\mathfrak{F}}^i\right) = J^e\boldsymbol{a}^i\cdot\mathcal{I}_N\left(\mathfrak{F}\right).$$

After some simple manipulations, for either the elastic-acoustic case or the electromagnetic case, one has

$$\int_{\hat{\mathsf{D}},N}\left(\mathcal{I}_N\left(\tilde{\mathfrak{F}}\mathfrak{q}^e\right)\cdot\nabla_{\boldsymbol{r}}\mathfrak{p}^e - \nabla_{\boldsymbol{r}}\cdot\mathcal{I}_N\left(\tilde{\mathfrak{F}}\mathfrak{q}^e\right)\cdot\mathfrak{p}^e\right) d\boldsymbol{r} = 0.$$

As a result, the volume terms vanish and the preceding equation can be expressed in the integrals over physical space as

$$\sum_e \frac{d}{dt}\mathcal{E}_d^e = -\sum_e \int_{\partial \mathsf{D}^e,N} \boldsymbol{n}\cdot\left[(\mathfrak{F}\mathfrak{q}^e)^* - \frac{1}{2}\mathfrak{F}\mathfrak{q}^e\right]\cdot\mathfrak{p}^e\,d\boldsymbol{x} + \sum_e \int_{\mathsf{D}^e,N}\mathfrak{g}^e\cdot\mathfrak{p}^e\,d\boldsymbol{x}. \quad (4.2)$$

Next, if $\partial\mathsf{D}^e \cap \partial\mathsf{D}^{e'}$ is a non-empty two-dimensional intersection ($\partial\mathsf{D}^e \cap \partial\mathsf{D}^{e'}$ has non-zero two-dimensional Lebesgue measure) we combine the integrands of the surface integrals on both "−" and "+" LGL (or LG) points. This is possible due to the mesh conformity, i.e., the number of LGL (or LG) points on "−" and "+" sides are the same and they can be reordered to be exactly coincident. After some algebraic manipulations for the surface integrals on the right side of (4.2), the following holds for the elastic–acoustic case:

$$\begin{aligned}\sum_e \frac{d}{dt}\mathcal{E}_d^e = -\frac{1}{2}\sum_e \int_{\partial\mathsf{D}^e,N} k_0\left\{(\boldsymbol{n}\cdot[\![\boldsymbol{S}]\!])^2 + \rho^-c_p^-\rho^+c_p^+\,[\![\boldsymbol{v}]\!]^2\right\}\\ + k_1\left\{\|\boldsymbol{n}\times(\boldsymbol{n}\times[\![\boldsymbol{S}]\!])\|^2 + +\rho^-c_s^-\rho^+c_s^+\,\|\boldsymbol{n}\times(\boldsymbol{n}\times[\boldsymbol{v}])\|^2\right\}d\boldsymbol{x}\\ + \sum_e \int_{\mathsf{D}^e,N}\mathfrak{g}^e\cdot\mathfrak{p}^e\,d\boldsymbol{x}, \quad (4.3)\end{aligned}$$

where terms involving k_1 are zero for a face either on or adjacent to the acoustic side. Similarly, for the electromagnetic case

$$\begin{aligned}\sum_e \frac{d}{dt}\mathcal{E}_d^e = \sum_e \int_{\mathsf{D}^e,N}\mathfrak{g}^e\cdot\mathfrak{p}^e\,d\boldsymbol{x}\\ - \frac{1}{2}\sum_e \int_{\partial\mathsf{D}^e,N}\frac{1}{2\,\{\{Z\}\}}\|\boldsymbol{n}\times\boldsymbol{n}\times[\boldsymbol{E}]\|^2 + \frac{1}{2\,\{\{Y\}\}}\|\boldsymbol{n}\times\boldsymbol{n}\times[\boldsymbol{H}]\|^2\,d\boldsymbol{x}, \quad (4.4)\end{aligned}$$

where terms involving $\boldsymbol{E}$ and $\boldsymbol{H}$ vanish for PMC and PEC boundaries, respectively, and both vanish for dielectric boundaries.

Now, for $\mathfrak{g} = 0$ we obtain from either (4.3) or (4.4) that the overall energy is non-increasing, i.e.,

$$\frac{d}{dt}\mathcal{E}_d \le 0.$$

For $\mathfrak{g} \neq 0$, we obtain the following estimate, by Cauchy-Schwarz and Young inequalities,

$$\frac{d}{dt}\mathcal{E}_d \le \int_{\mathcal{D}^{N_{\mathrm{el}}}}\mathfrak{g}\cdot\mathfrak{p} \le \frac{1}{2}\left(\mathcal{E}_d + \|\mathcal{I}_N\boldsymbol{g}\|^2_{\mathcal{D}^{N_{\mathrm{el}}},d}\right).$$

□

5. Mortar-based non-conforming approximations.

In this section, we employ the mortar-based approximation idea proposed by Kopriva *et al.* [18, 22]. However, we propose to use a discretized mortar-based approximation to show stability in addition to the outflow condition and global conservation as required by the original mortar method [18, 22]. As will be shown, our discrete version requires a special quadrature rule in order to simultaneously satisfy

all the requirements. We provide a setting that allows unified proofs that are valid for both functional (due to order refinement) and geometric (due to local subdivision) non-conforming approximations.

The following conventions are adopted. We use bold face type to denote vectors of nodal values of the corresponding quantities under consideration. For example, $\mathbf{q}$ is the vector of nodal values of $\mathfrak{q}$. In addition, we use upper case script type to denote matrices, e.g. $\mathscr{P}$.

We consider non-conforming approximations due to domain subdivision in which elements may be subdivided locally while their neighbors may not. For simplicity of exposition, we further restrict ourselves to the case where a subdomain interface between two adjacent elements (two elements are said to be *adjacent* to each other if their boundary intersection has non-zero two-dimensional Lebesgue measure) must be an entire face of either of them. Nevertheless, adjacent elements are allowed to have different solution orders, and hence order refinement (i.e., p-refinement) in addition to domain subdivision (i.e., h-refinement) is permissible. From here on, by "non-conforming interface" we mean that an entire face of one element is also a union of faces of other adjacent elements (h-non-conforming), or, the solution orders of two elements sharing a face are different (p-non-conforming). A non-conforming interface with one element on one side and seven elements on the other side is shown in Figure 5.1.

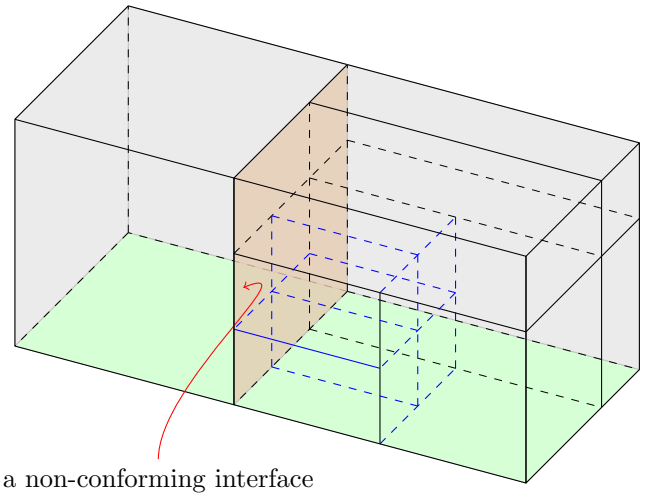

FIG. 5.1. *A non-conforming interface with one hexahedron on one side and seven hexahedra on the other side.*

Consider a non-conforming interface where on the "−" side is face f_{e_0} of element e_0 and on the "+" side are faces f_{e_i} of elements $e_i, i = 1, \ldots, N_a$. Clearly, this setting includes both kinds of non-conforming interfaces. We create N_a mortars $\mathcal{M}_i, i = 1, \ldots, N_a$ whose "−" sides are seen by element e_0 and "+" sides by elements e_i, respectively. As in [22], the geometric order on the mortars must be the lowest geometric order of the contributing elements, and the polynomial should be defined along face f_{e_0}. This will ensure that the mortars match sub-interfaces between elements exactly, and hence the metrics $J^{e_i}\boldsymbol{a}^{e_i}$ on a mortar and the corresponding contributing element faces are represented by identical polynomials. The solution orders of the mortars are chosen as $N_{m_i} \geq \max\{N_{e_0}, N_{e_i}\}$ which is sufficient to satisfy the outflow

condition, as we shall show. An example with seven mortars corresponding to the non-conforming interface in Figure 5.1 is shown in Figure 5.2.

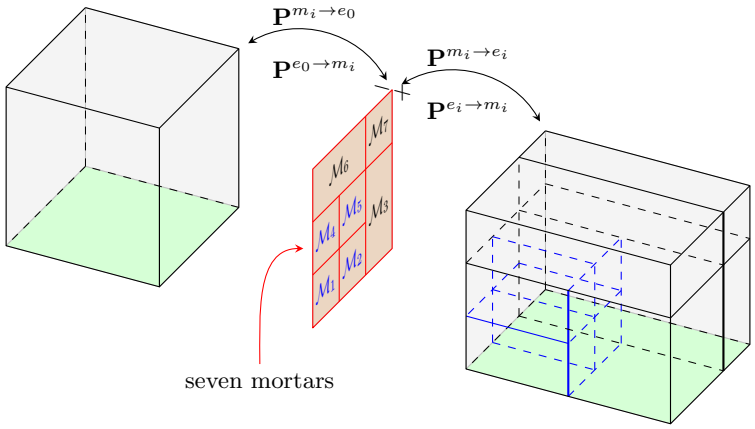

FIG. 5.2. *Seven mortars corresponding to the non-conforming interface in Figure 5.1.*

The goal of the mortar approximation is to compute the contravariant fluxes on faces $f_{e_i}, i = 0, \ldots, N_a$. This is a three-step process. First, the states on e_0 and e_i are projected on the mortars through L^2 projectors $\mathscr{P}^{e_0 \to m_i}$ and $\mathscr{P}^{e_i \to m_i}$, $i = 1, \ldots, N_a$. The projected states are then used to compute the mortar contravariant fluxes as if each mortar is a conforming face. The final step is to project the contravariant fluxes back on the element faces using projectors $\mathscr{P}^{m_i \to e_0}$ and $\mathscr{P}^{m_i \to e_i}$. The illustration of steps 1 and 3 can be seen in Figure 5.2. The components of each step are now detailed.

State $\mathfrak{q}^{m_i^-}$ on the "$-$" side of mortar $\mathcal{M}_i$ is the least squares projection of state $\mathfrak{q}^{e_0}$ from element e_0 onto space $\mathcal{P}_{N_{m_i}}$, i.e.,

$$\begin{aligned}
&\int_{\mathcal{M}_i} \mathfrak{q}^{m_i^-}(\boldsymbol{r})\, \boldsymbol{\ell}_k^{m_i}(\boldsymbol{r})\, d\boldsymbol{r} = \\
&\int_{\mathcal{M}_i} \mathfrak{q}^{e_0}\left(\left(\boldsymbol{X}^{e_0}\right)^{-1} \circ \boldsymbol{X}^{e_i}(\boldsymbol{r}) \right) \boldsymbol{\ell}_k^{m_i}(\boldsymbol{r})\, d\boldsymbol{r}, \quad \forall \boldsymbol{\ell}_k^{m_i}(\boldsymbol{r}) \in \mathcal{P}_{N_{m_i}}.
\end{aligned} \tag{5.1}$$

Since our main goal is to prove semi-stability, least squares projection of the type (5.1) is approximated using quadratures. Nevertheless, we do not wish to violate the outflow condition and global conservation. In fact, the outflow condition is necessary to ensure stability, as shown in Section 6. In this paper, the following quadrature rule is used. For any surface integral in the least squares projection of the type (5.1), the quadrature rule is chosen to correspond to the integrand with the highest order. For example, the N_{m_i}th-order quadrature rule is used for both integrals in (5.1). Explicitly, we approximate (5.1) as

$$\begin{aligned}
&\int_{\mathcal{M}_i, N_{m_i}} \mathfrak{q}^{m_i^-}(\boldsymbol{r})\, \boldsymbol{\ell}_k^{m_i}(\boldsymbol{r})\, d\boldsymbol{r} = \\
&\int_{\mathcal{M}_i, N_{m_i}} \mathfrak{q}^{e_0}\left(\left(\boldsymbol{X}^{e_0}\right)^{-1} \circ \boldsymbol{X}^{e_i}(\boldsymbol{r}) \right) \boldsymbol{\ell}_k^{m_i}(\boldsymbol{r})\, d\boldsymbol{r}, \quad \forall \boldsymbol{\ell}_k^{m_i}(\boldsymbol{r}) \in \mathcal{P}_{N_{m_i}},
\end{aligned} \tag{5.2}$$

206 which yields

$$\mathbf{q}^{m_i^-} = \underbrace{\left(\mathscr{M}^{m_i}\right)^{-1}\mathscr{R}^{e_0\to m_i}}_{\mathscr{P}^{e_0\to m_i}}\mathbf{q}^{e_0}$$

where the matrices $\mathscr{M}^{m_i}$ and $\mathscr{R}^{e_0\to m_i}$ are defined as

$$\mathscr{M}^{m_i}_{k_1,k_2} = \int_{\mathcal{M}_i,N_{m_i}} \boldsymbol{\ell}^{m_i}_{k_1}(\boldsymbol{r})\,\boldsymbol{\ell}^{m_i}_{k_2}(\boldsymbol{r})\,d\boldsymbol{r},$$
$$\mathscr{R}^{e_0\to m_i}_{k,j} = \int_{\mathcal{M}_i,N_{m_i}} \boldsymbol{\ell}^{m_i}_{k}(\boldsymbol{r})\,\boldsymbol{\ell}^{e_0}_{j}\left(\left(\boldsymbol{X}^{e_0}\right)^{-1}\circ\boldsymbol{X}^{e_i}(\boldsymbol{r})\right)d\boldsymbol{r},\quad \forall\boldsymbol{\ell}^{e_0}_j\in\mathcal{P}_{N_{e_0}}.$$

Similarly, the least squares projection of state $\mathfrak{q}^{e_i}$ from element e_i onto $\mathcal{P}_{N_{m_i}}$ is state $\mathfrak{q}^{m_i^+}$ on the "+" side of mortar $\mathcal{M}_i$. Using the above quadrature rule we have

$$\int_{\mathcal{M}_i,N_{m_i}} \mathfrak{q}^{m_i^+}(\boldsymbol{r})\,\boldsymbol{\ell}^{m_i}_k(\boldsymbol{r})\,d\boldsymbol{r} =$$
$$\int_{\mathcal{M}_i,N_{m_i}} \mathfrak{q}^{e_i}(\boldsymbol{r})\,\boldsymbol{\ell}^{m_i}_k(\boldsymbol{r})\,d\boldsymbol{r},\quad \forall\boldsymbol{\ell}^{m_i}_k(\boldsymbol{r})\in\mathcal{P}_{N_{m_i}}, \tag{5.3}$$

207 or, equivalently,

$$\mathbf{q}^{m_i^+} = \underbrace{\left(\mathscr{M}^{m_i}\right)^{-1}\mathscr{R}^{e_i\to m_i}}_{\mathscr{P}^{e_i\to m_i}}\mathbf{q}^{e_i} \tag{5.4}$$

with $\mathscr{R}^{e_i\to m_i}$ defined as

$$\mathscr{R}^{e_i\to m_i}_{k,j} = \int_{\mathcal{M}_i,N_{m_i}} \boldsymbol{\ell}^{m_i}_{k}(\boldsymbol{r})\,\boldsymbol{\ell}^{e_i}_{j}(\boldsymbol{r})\,d\boldsymbol{r},\quad \forall\boldsymbol{\ell}^{e_i}_j\in\mathcal{P}_{N_{e_i}}.$$

Since the fluxes depend on λ,μ,ε, and μ, we perform the above least squares projection procedure on them as well. Based on the projected states $\mathfrak{q}^{m_i^-}$, $\mathfrak{q}^{m_i^+}$, and projected coefficients, we compute the contravariant Riemann fluxes $\tilde{\mathfrak{F}}^*_{m_i} = \left(\tilde{\boldsymbol{n}}\cdot\tilde{\mathfrak{F}}\left(\mathfrak{q}^{m_i}\right)\right)^*$ on the mortars as if the mortars are conforming faces. This is done using a simple relation between the contravariant and covariant Riemann fluxes as in [20]. The projected states are also used to compute the contravariant fluxes $\tilde{\mathfrak{F}}^-_{m_i} = \tilde{\boldsymbol{n}}\cdot\tilde{\mathfrak{F}}\left(\mathfrak{q}^{m_i^-}\right)$, and $\tilde{\mathfrak{F}}^+_{m_i} = \tilde{\boldsymbol{n}}\cdot\tilde{\mathfrak{F}}\left(\mathfrak{q}^{m_i^+}\right)$. The final step is to project the mortar contravariant fluxes $\tilde{\mathfrak{F}}^*_{m_i},\tilde{\mathfrak{F}}^-_{m_i}$ and $\tilde{\mathfrak{F}}^+_{m_i}$ onto $\mathcal{P}_{N_{e_i}}, i=0,\ldots,N_a$. Since the procedure is the same for $\tilde{\mathfrak{F}}^*_{m_i},\tilde{\mathfrak{F}}^-_{m_i}$ and $\tilde{\mathfrak{F}}^+_{m_i}$, we describe only the process of projecting $\tilde{\mathfrak{F}}^*_{m_i}$ to obtain the contravariant fluxes $\tilde{\mathfrak{F}}^*_{e_i}$ on faces f_{e_i} of the contributing elements. The discretized least squares projection using the quadrature rule discussed above for face f_{e_0} is as follows:

$$\int_{f_{e_0},N_{e_0}} \tilde{\mathfrak{F}}^*_{e_0}(\boldsymbol{r})\,\boldsymbol{\ell}^{e_0}_j(\boldsymbol{r})\,d\boldsymbol{r} =$$
$$\sum_{i=1}^{N_a}\int_{\mathcal{M}_i,N_{m_i}} \tilde{\mathfrak{F}}^*_{m_i}(\boldsymbol{r})\,\boldsymbol{\ell}^{e_0}_j\left(\left(\boldsymbol{X}^{e_0}\right)^{-1}\circ\boldsymbol{X}^{e_i}(\boldsymbol{r})\right)d\boldsymbol{r},\quad \forall\boldsymbol{\ell}^{e_0}_j\in\mathcal{P}_{N_{e_0}}, \tag{5.5}$$

for which, in matrix notation, the vector of nodal values of $\tilde{\mathfrak{F}}^*_{e_0}$, $\tilde{\mathbf{F}}^*_{e_0}$, is computed as

$$\mathscr{M}^{e_0}\tilde{\mathbf{F}}^*_{e_0} = \sum_{i=1}^{N_a} \mathscr{R}^{m_i\to e_0}\tilde{\mathbf{F}}^*_{m_i},$$

or in terms of projection matrices,

$$\tilde{\mathbf{F}}^*_{e_0} = \sum_{i=1}^{N_a} \underbrace{\left(\mathscr{M}^{e_0}\right)^{-1}\mathscr{R}^{m_i\to e_0}}_{\mathscr{P}^{m_i\to e_0}}\tilde{\mathbf{F}}^*_{m_i}, \tag{5.6}$$

where

$$\mathscr{M}^{e_0}_{k,j} = \int_{\mathcal{M}_i,N_{e_0}} \boldsymbol{\ell}^{e_0}_k(\boldsymbol{r})\,\boldsymbol{\ell}^{e_0}_j(\boldsymbol{r})\,d\boldsymbol{r}, \quad \mathscr{R}^{m_i\to e_0} = \left(\mathscr{R}^{e_0\to m_i}\right)^T. \tag{5.7}$$

Similarly, the vector of nodal values of $\tilde{\mathfrak{F}}^-_{e_0}$, $\tilde{\mathbf{F}}^-_{e_0}$ is given by

$$\tilde{\mathbf{F}}^-_{e_0} = \sum_{i=1}^{N_a} \mathscr{P}^{m_i\to e_0}\tilde{\mathbf{F}}^-_{m_i}. \tag{5.8}$$

The projection to compute contravariant fluxes $\tilde{\mathfrak{F}}^*_{e_i}$ on surface f_{e_i} $i = 1,\ldots,N_a$ of other contributing elements is simpler,

$$\begin{aligned}&\int_{\mathcal{M}_i,N_{e_i}} \tilde{\mathfrak{F}}^*_{e_i}(\boldsymbol{r})\,\boldsymbol{\ell}^{e_i}_j(\boldsymbol{r})\,d\boldsymbol{r} = \\ &\int_{\mathcal{M}_i,N_{m_i}} \tilde{\mathfrak{F}}^*_{m_i}(\boldsymbol{r})\,\boldsymbol{\ell}^{e_i}_j(\boldsymbol{r})\,d\boldsymbol{r} = 0, \quad \forall \boldsymbol{\ell}^{e_i}_j(\boldsymbol{r}) \in \mathcal{P}_{N_{e_i}},\end{aligned} \tag{5.9}$$

which yields

$$\tilde{\mathbf{F}}^*_{e_i} = \underbrace{\left(\mathscr{M}^{e_i}\right)^{-1}\mathscr{R}^{m_i\to e_i}}_{\mathscr{P}^{m_i\to e_i}}\tilde{\mathbf{F}}^*_{m_i}, \tag{5.10}$$

where

$$\mathscr{M}^{e_i}_{k,j} = \int_{\mathcal{M}_i,N_{e_i}} \boldsymbol{\ell}^{e_i}_k(\boldsymbol{r})\,\boldsymbol{\ell}^{e_i}_j(\boldsymbol{r})\,d\boldsymbol{r}, \quad \mathscr{R}^{m_i\to e_i} = \left(\mathscr{R}^{e_i\to m_i}\right)^T. \tag{5.11}$$

Similarly,

$$\tilde{\mathbf{F}}^+_{e_i} = \mathscr{P}^{m_i\to e_i}\tilde{\mathbf{F}}^+_{m_i}. \tag{5.12}$$

Recall that the outflow condition means the invariance of a polynomial function when projected to the mortars and back to the face [18, 22]. We are now in a position to discuss the outflow condition for the above discrete mortar-based approximation.

PROPOSITION 1. *Assume $N_{m_i} \geq \max\{N_{e_0}, N_{e_i}\}$, $i = 1,\ldots,N_a$. Then the discrete mortar-based approximation with LG quadrature satisfies the strong outflow conditions, namely,*

$$\mathscr{P}^{m_i\to e_i}\mathscr{P}^{e_i\to m_i} = \boldsymbol{I}, \quad i = 1,\ldots,N_a, \tag{5.13}$$

$$\sum_{i=1}^{N_a} \mathscr{P}^{m_i\to e_0}\mathscr{P}^{e_0\to m_i} = \boldsymbol{I}, \tag{5.14}$$

where $\boldsymbol{I}$ *is the identity matrix of appropriate size. On the other hand, discretizations using LGL quadrature satisfy only the outflow condition in the following weak sense,*

$$\int_{\mathcal{M}_i,N_{m_i}} \mathfrak{q}^{e_i}(\boldsymbol{r})\,\hat{\boldsymbol{\ell}}\,d\boldsymbol{r} = \int_{\mathcal{M}_i,N_{e_i}} \hat{\mathfrak{q}}^{e_i}(\boldsymbol{r})\,\hat{\boldsymbol{\ell}}\,d\boldsymbol{r}, \quad \forall \hat{\boldsymbol{\ell}} \in \mathcal{P}_{N_{e_i}}, \tag{5.15}$$

and

$$\sum_{i=1}^{N_a} \int_{\mathcal{M}_i,N_{m_i}} \mathfrak{q}^{e_0}\left((\boldsymbol{X}^{e_0})^{-1}\circ \boldsymbol{X}^{e_i}(\boldsymbol{r})\right)\hat{\boldsymbol{\ell}}\left((\boldsymbol{X}^{e_0})^{-1}\circ \boldsymbol{X}^{e_i}(\boldsymbol{r})\right)\,d\boldsymbol{r} = \int_{f_{e_0},N_{e_0}} \hat{\mathfrak{q}}^{e_0}(\boldsymbol{r})\,\hat{\boldsymbol{\ell}}(\boldsymbol{r})\,d\boldsymbol{r}, \quad \forall \hat{\boldsymbol{\ell}} \in \mathcal{P}_{N_{e_0}}, \tag{5.16}$$

where $\hat{\mathfrak{q}}^{e_i}$ *is the result from the projection of* $\mathfrak{q}^{e_i}$ *to* $\mathcal{M}_i$ *and back on* f_{e_i}*, and* $\hat{\mathfrak{q}}^{e_0}$ *the result from the projection of* $\mathfrak{q}^{e_0}$ *to* $\mathcal{M}_i$ *and back on* f_{e_0}*.*

Proof. We first show (5.13). Denote $\mathbf{q}^{m_i^+}$ as the projection of $\mathbf{q}^{e_i}$ on mortar $\mathcal{M}_i$, using (5.3) and (5.9), we have

$$\int_{\mathcal{M}_i,N_{m_i}} \mathfrak{q}^{m_i^+}(\boldsymbol{r})\,\boldsymbol{\ell}(\boldsymbol{r})\,d\boldsymbol{r} = \int_{\mathcal{M}_i,N_{m_i}} \mathfrak{q}^{e_i}(\boldsymbol{r})\,\boldsymbol{\ell}(\boldsymbol{r})\,d\boldsymbol{r}, \quad \forall \boldsymbol{\ell} \in \mathcal{P}_{N_{m_i}},$$
$$\int_{\mathcal{M}_i,N_{m_i}} \mathfrak{q}^{m_i^+}(\boldsymbol{r})\,\hat{\boldsymbol{\ell}}(\boldsymbol{r})\,d\boldsymbol{r} = \int_{\mathcal{M}_i,N_{e_i}} \hat{\mathfrak{q}}^{e_i}(\boldsymbol{r})\,\hat{\boldsymbol{\ell}}(\boldsymbol{r})\,d\boldsymbol{r}, \quad \forall \hat{\boldsymbol{\ell}} \in \mathcal{P}_{N_{e_i}} \subset \mathcal{P}_{N_{m_i}},$$

which imply the weak outflow condition (5.15). This weak outflow condition is valid for both LGL and LG quadrature rules. For LG quadrature, however, the weak outflow condition also implies the strong one, namely, $\hat{\mathbf{q}}^{e_i} = \mathbf{q}^{e_i}$, and hence (5.13), since LG quadrature is exact.

For (5.14), denote $\hat{\mathfrak{q}}^{m_i^-}$ as the projection of $\mathfrak{q}^{e_0}$ onto mortars $\mathcal{M}_i$. Equations (5.2) and (5.5) imply, for $i = 1,\ldots,N_a$,

$$\int_{\mathcal{M}_i,N_{m_i}} \mathfrak{q}^{m_i^-}(\boldsymbol{r})\,\boldsymbol{\ell}(\boldsymbol{r})\,d\boldsymbol{r} =$$
$$\int_{\mathcal{M}_i,N_{m_i}} \mathfrak{q}^{e_0}\left((\boldsymbol{X}^{e_0})^{-1}\circ \boldsymbol{X}^{e_i}(\boldsymbol{r})\right)\boldsymbol{\ell}(\boldsymbol{r})\,d\boldsymbol{r}, \quad \forall \boldsymbol{\ell} \in \mathcal{P}_{N_{m_i}}, \tag{5.17}$$
$$\sum_{j=1}^{N_a} \int_{\mathcal{M}_j,N_{m_j}} \mathfrak{q}^{m_j^-}(\boldsymbol{r})\,\hat{\boldsymbol{\ell}}\left((\boldsymbol{X}^{e_0})^{-1}\circ \boldsymbol{X}^{e_j}(\boldsymbol{r})\right)\,d\boldsymbol{r} =$$
$$\int_{f_{e_0},N_{e_0}} \hat{\mathfrak{q}}^{e_0}(\boldsymbol{r})\,\hat{\boldsymbol{\ell}}(\boldsymbol{r})\,d\boldsymbol{r}, \quad \forall \hat{\boldsymbol{\ell}} \in \mathcal{P}_{N_{e_0}}. \tag{5.18}$$

Since $N_{m_i} \geq \max\{N_{e_0}, N_{e_i}\}$, and hence $\mathcal{P}_{N_{e_0}} \subset \mathcal{P}_{N_{m_i}}$, $i = 1,\ldots,N_a$, we take $\boldsymbol{\ell}(\boldsymbol{r}) = \hat{\boldsymbol{\ell}}\left((\boldsymbol{X}^{e_0})^{-1}\circ \boldsymbol{X}^{e_i}(\boldsymbol{r})\right)$ in (5.17) and sum over $i = 1,\ldots,N_a$, and finally subtract from (5.18) to obtain the weak outflow condition (5.16). Again, by the exactness of LG quadrature we have $\hat{\mathbf{q}}^{e_0} = \mathbf{q}^{e_0}$, and hence (5.14). ∎

PROPOSITION 2. *The discrete mortar-based approximation satisfies the following global conservation,*

$$\int_{f_{e_0}} \tilde{\mathfrak{F}}^*_{e_0}\,d\boldsymbol{r} = \sum_{i=1}^{N_a} \int_{f_{e_i}} \tilde{\mathfrak{F}}^*_{e_i}\,d\boldsymbol{r}.$$

Proof. This result is an easy consequence of (5.5) and (5.9). Indeed, taking $\boldsymbol{\ell}^{e_0} \equiv 1$ in (5.5) and $\boldsymbol{\ell}_j^{e_i} \equiv 1$ in (5.9), we have

$$\int_{f_{e_0},N_{e_0}} \tilde{\mathfrak{F}}^*_{e_0}(\boldsymbol{r})\, d\boldsymbol{r} = \sum_{i=1}^{N_a} \int_{\mathcal{M}_i,N_{m_i}} \tilde{\mathfrak{F}}^*_{m_i}(\boldsymbol{r})\, d\boldsymbol{r},$$

and

$$\sum_{i=1}^{N_a} \int_{\mathcal{M}_i,N_{e_i}} \tilde{\mathfrak{F}}^*_{e_i}(\boldsymbol{r})\, d\boldsymbol{r} = \sum_{i=1}^{N_a} \int_{\mathcal{M}_i,N_{m_i}} \tilde{\mathfrak{F}}^*_{m_i}(\boldsymbol{r})\, d\boldsymbol{r}.$$

Observe that $\tilde{\mathfrak{F}}^*_{e_0}(\boldsymbol{r})$ is a polynomial of order at most N_{e_0}, while $\tilde{\mathfrak{F}}^*_{e_i}(\boldsymbol{r})$ is a polynomial of order at most N_{e_i}. The exactness of either LGL or LG quadrature completes the proof. □

6. Semi-discrete stability for non-conforming meshes. We start this section with a discussion on why the outflow condition is necessary for the stability proof to hold. The semi-discrete form (3.2) is also applied for non-conforming approximation using the mortar method in Section 5. However, the contravariant fluxes $\left(\tilde{\mathfrak{F}}\mathfrak{q}^e\right)^*$ and $\tilde{\mathfrak{F}}\mathfrak{q}^e$ on the boundary $\partial\hat{\mathsf{D}}$ are the projected values of the mortar contravariant fluxes instead of the trace of the flux $\tilde{\mathfrak{F}}\mathfrak{q}^e$. Accordingly, using commutativity of quadrature and integration by parts [29, 21], (3.2) becomes

$$\begin{aligned}&\sum_e \int_{\hat{\mathsf{D}},N_e} J^e \mathcal{Q}^e \frac{\partial \mathfrak{q}^e}{\partial t} \cdot \mathfrak{p}^e\, d\boldsymbol{r} - \sum_e \int_{\hat{\mathsf{D}},N_e} \mathcal{I}_{N_e}\left(\tilde{\mathfrak{F}}\mathfrak{q}^e\right) \cdot \nabla_{\boldsymbol{r}} \cdot \mathfrak{p}^e\, d\boldsymbol{r} \\ &+ \sum_e \int_{\partial\hat{\mathsf{D}},N_e} \tilde{\boldsymbol{n}} \cdot \left[\left(\tilde{\mathfrak{F}}\mathfrak{q}^e\right)^* - \tilde{\mathfrak{F}}\mathfrak{q}^e + \left.\tilde{\mathfrak{F}}\mathfrak{q}^e\right|_{\partial\hat{\mathsf{D}}}\right] \cdot \mathfrak{p}^e\, d\boldsymbol{r} = \sum_e \int_{\hat{\mathsf{D}},N_e} J^e \mathfrak{g}^e \cdot \mathfrak{p}^e\, d\boldsymbol{r}, \quad (6.1)\end{aligned}$$

where $\left.\tilde{\mathfrak{F}}\mathfrak{q}^e\right|_{\partial\hat{\mathsf{D}}}$ is the trace of the flux $\tilde{\mathfrak{F}}\mathfrak{q}^e$ on $\partial\hat{\mathsf{D}}$. For the conforming approximation, one has $\left.\tilde{\mathfrak{F}}\mathfrak{q}^e\right|_{\partial\hat{\mathsf{D}}} - \tilde{\mathfrak{F}}\mathfrak{q}^e = 0, \forall \boldsymbol{r} \in \partial\hat{\mathsf{D}}$, and this is the reason why (4.1) holds. This no longer holds for the non-conforming approximation unless $\tilde{\mathfrak{F}}\mathfrak{q}^e = \left.\tilde{\mathfrak{F}}\mathfrak{q}^e\right|_{\partial\hat{\mathsf{D}}}, \forall \boldsymbol{r} \in \partial\hat{\mathsf{D}}$, which is true if the outflow condition is satisfied and $\tilde{\mathfrak{F}}\mathfrak{q}^e \in \mathcal{P}_{N^e}$.

We introduce the global interpolation operator Π whose restriction on element D^e is

$$\Pi|_{\mathsf{D}^e} = \mathcal{I}_{N_e},$$

which allows us to obtain the following stability proof for our non-conforming approximation.

THEOREM 2. *Assume*

(i) The discrete mortar approach in Section 5 is used for non-conforming approximations.

(ii) The mesh is affine.

(iii) The LG quadrature is used, i.e., the strong outflow condition is satisfied.

(iv) $\mathfrak{F}\mathfrak{q}^e \in \mathcal{P}_{N^e}$.

Then the DGSEM discretization is stable in the sense that

$$\frac{d}{dt}\mathcal{E}_d \leq \frac{1}{2}\left(\mathcal{E}_d + \|\Pi \mathfrak{g}\|^2_{\mathcal{D}^{N_{el}},d}\right).$$

Moreover, if $\mathfrak{g} = 0$*, then* $\frac{d}{dt}\mathcal{E}_d \leq 0$.

Proof. As discussed above, assumptions (iii) and (iv) imply the identity $\tilde{\mathfrak{F}}\mathfrak{q}^e\Big|_{\partial\hat{\mathsf{D}}} - \tilde{\mathfrak{F}}\mathfrak{q}^e = 0, \forall \boldsymbol{r} \in \partial\hat{\mathsf{D}}$. Therefore, similar to the proof of Theorem 1, we substitute $\mathfrak{p} := \begin{pmatrix} \boldsymbol{S} \\ \boldsymbol{v} \end{pmatrix} := \begin{pmatrix} \mathsf{C}\boldsymbol{E} \\ \boldsymbol{v} \end{pmatrix}$ for the elastic-acoustic case and $\mathfrak{p} = \mathfrak{q}$ for the electromagnetic case, to obtain

$$\sum_e \frac{d}{dt}\mathcal{E}^e_d = \sum_e -\int_{\partial\hat{\mathsf{D}},N_e} \tilde{\boldsymbol{n}} \cdot \left[\left(\tilde{\mathfrak{F}}\mathfrak{q}^e\right)^* - \frac{1}{2}\left(\tilde{\mathfrak{F}}\mathfrak{q}^e\right)\right] \cdot \mathfrak{p}^e \, d\boldsymbol{r} + \sum_e \int_{\hat{\mathsf{D}},N_e} J^e \mathfrak{g}^e \cdot \mathfrak{p}^e \, d\boldsymbol{r}. \quad (6.2)$$

We divide the surface integrals into two groups, namely, surface integrals associated with conforming and with non-conforming interfaces. The former group has been shown to be non-positive as in the proof of Theorem 1. We therefore need to consider only the latter group for which we take a typical non-conforming interface and its contributing surface integrals as in Section 5. We shall show that the non-conforming contribution is also non-positive.

The surface integral contributed from element e_0, with the contravariant fluxes projected from mortars, can be written as

$$\begin{aligned}
&-\textstyle\int_{f_{e_0},N^{e_0}} \left[\tilde{\mathfrak{F}}^*_{e_0} - \frac{1}{2}\tilde{\mathfrak{F}}^-_{e_0}\right] \cdot \mathfrak{p}^{e_0} \, d\boldsymbol{r} \\
&= -\left(\mathbf{p}^{e_0}\right)^T \mathbf{M}^{e_0} \left[\tilde{\mathbf{F}}^*_{e_0} - \tfrac{1}{2}\tilde{\mathbf{F}}^-_{e_0}\right] && \text{using quadrature} \\
&= -\textstyle\sum_{i=1}^{N_a} \left(\mathbf{p}^{e_0}\right)^T \mathscr{R}^{m_i \to e_0} \left[\tilde{\mathbf{F}}^*_{m_i} - \tfrac{1}{2}\tilde{\mathbf{F}}^-_{m_i}\right] && \text{using (5.6) and (5.8)} \\
&= -\textstyle\sum_{i=1}^{N_a} \left(\mathbf{p}^{m_i^-}\right)^T \mathscr{M}^{m_i} \left[\tilde{\mathbf{F}}^*_{m_i} - \tfrac{1}{2}\tilde{\mathbf{F}}^-_{m_i}\right] && \text{using (5.3) and (5.7)} \\
&= -\textstyle\sum_{i=1}^{N_a} \int_{\mathcal{M}_i,N_{m_i}} \left[\tilde{\mathfrak{F}}^*_{m_i} - \frac{1}{2}\tilde{\mathfrak{F}}^-_{m_i}\right] \cdot \mathfrak{p}^{m_i^-} \, d\boldsymbol{r} && \text{using quadrature} \\
&= -\textstyle\sum_{i=1}^{N_a} \int_{\mathcal{M}_i,N_{m_i}} \tilde{\boldsymbol{n}} \cdot \left[\left(\tilde{\mathfrak{F}}\left(\mathfrak{q}^{m_i}\right)\right)^* - \frac{1}{2}\tilde{\mathfrak{F}}\left(\mathfrak{q}^{m_i^-}\right)\right] \cdot \mathfrak{p}^{m_i^-} \, d\boldsymbol{r}. && \text{by definition}
\end{aligned}$$

For each contributing element $e_i, i = 1, \ldots, N_a$, the surface integral on face f_{e_i}, with the contravariant fluxes projected from mortars, is

$$\begin{aligned}
&-\textstyle\int_{f_{e_i},N^{e_i}} \left[\tilde{\mathfrak{F}}^*_{e_i} - \frac{1}{2}\tilde{\mathfrak{F}}^-_{e_i}\right] \cdot \mathfrak{p}^{e_i} \, d\boldsymbol{r} \\
&= -\left(\mathbf{p}^{e_i}\right)^T \mathbf{M}^{e_i} \left[\tilde{\mathbf{F}}^*_{e_i} - \tfrac{1}{2}\tilde{\mathbf{F}}^-_{e_i}\right] && \text{using quadrature} \\
&= -\left(\mathbf{p}^{e_i}\right)^T \mathscr{R}^{m_i \to e_i} \left[\tilde{\mathbf{F}}^*_{m_i} - \tfrac{1}{2}\tilde{\mathbf{F}}^+_{m_i}\right] && \text{using (5.10) and (5.12)} \\
&= -\left(\mathbf{p}^{m_i^+}\right)^T \mathscr{M}^{m_i} \left[\tilde{\mathbf{F}}^*_{m_i} - \tfrac{1}{2}\tilde{\mathbf{F}}^+_{m_i}\right] && \text{using (5.4) and (5.11)} \\
&= -\textstyle\int_{\mathcal{M}_i,N_{m_i}} \left[\tilde{\mathfrak{F}}^*_{m_i} - \frac{1}{2}\tilde{\mathfrak{F}}^+_{m_i}\right] \cdot \mathfrak{p}^{m_i^+} \, d\boldsymbol{r} && \text{using quadrature} \\
&= -\textstyle\int_{\mathcal{M}_i,N_{m_i}} \tilde{\boldsymbol{n}} \cdot \left[\left(\tilde{\mathfrak{F}}\left(\mathfrak{q}^{m_i}\right)\right)^* - \frac{1}{2}\tilde{\mathfrak{F}}\left(\mathfrak{q}^{m_i^+}\right)\right] \cdot \mathfrak{p}^{m_i^+} \, d\boldsymbol{r}. && \text{by definition}
\end{aligned}$$

Therefore, we have shown that each non-conforming interface consisting of faces f_{e_i} of contributing elements e_i, $i = 0, \ldots, N_a$, is equivalent to $2N_a$ conforming faces

associated with N_a mortars $\mathcal{M}_j$, $j = 1, \ldots, N_a$. That is, the surface integrals in (6.2) in fact consist of conforming interfaces—either the original conforming interfaces or equivalent conforming mortars. The stability proof of Theorem 1 for conforming faces can now be applied to complete the proof. □

When the strong outflow condition is not satisfied, i.e., when LGL quadrature is used as in Proposition 1. We have the following stability.

THEOREM 3. *Suppose all assumptions in Theorem 2 hold except that the LGL quadrature is employed. Then the DGSEM discretization is stable in the sense that*

$$\frac{d}{dt}\mathcal{E}_d \leq \frac{1}{2}\left((1+2c)\,\mathcal{E}_d + \|\Pi\mathfrak{g}\|^2_{\mathcal{D}^{N_{el}},d}\right),$$

where the small constant c converges to zero if the exact solution $\mathfrak{q}$ is sufficiently smooth.

Proof. When the numerical integration is not exact, we have the following extra term

$$\sum_e \int_{\partial\hat{\mathsf{D}},N_e} \tilde{\boldsymbol{n}} \cdot \left[\tilde{\mathfrak{F}}\mathfrak{q}^e\Big|_{\partial\hat{\mathsf{D}}} - \tilde{\mathfrak{F}}\mathfrak{q}^e\right] \cdot \mathfrak{p}^e \, d\boldsymbol{r},$$

which can be shown to be small as

$$\sum_e \int_{\partial\hat{\mathsf{D}},N_e} \tilde{\boldsymbol{n}} \cdot \left[\tilde{\mathfrak{F}}\mathfrak{q}^e\Big|_{\partial\hat{\mathsf{D}}} - \tilde{\mathfrak{F}}\mathfrak{q}^e\right] \cdot \mathfrak{p}^e \, d\boldsymbol{r} \leq c\mathcal{E}_d. \tag{6.3}$$

We now provide an explicit estimate for the constant c to show that c is indeed negligible. It is sufficient to estimate the error for contributing element e_i whose face f_{e_i} is on the "+" side of a mortar. From the weak outflow identity (5.15), we have

$$\begin{aligned}
&\left|\int_{e_i,N_{e_i}} \tilde{\boldsymbol{n}} \cdot \left[\tilde{\mathfrak{F}}\mathfrak{q}^{e_i}\Big|_{\partial\hat{\mathsf{D}}} - \tilde{\mathfrak{F}}\mathfrak{q}^{e_i}\right] \cdot \mathfrak{p}^{e_i} \, d\boldsymbol{r}\right| \leq \\
&\left|\int_{\mathcal{M}_i,N_{m_i}} \tilde{\boldsymbol{n}} \cdot \tilde{\mathfrak{F}}\mathfrak{q}^{e_i}\Big|_{\partial\hat{\mathsf{D}}} \cdot \mathfrak{p}^{e_i} \, d\boldsymbol{r} - \int_{\mathcal{M}_i} \tilde{\boldsymbol{n}} \cdot \tilde{\mathfrak{F}}\mathfrak{q}^{e_i}\Big|_{\partial\hat{\mathsf{D}}} \cdot \mathfrak{p}^{e_i} \, d\boldsymbol{r}\right| \\
&+ \left|\int_{\mathcal{M}_i,N_{e_i}} \tilde{\boldsymbol{n}} \cdot \tilde{\mathfrak{F}}\mathfrak{q}^{e_i}\Big|_{\partial\hat{\mathsf{D}}} \cdot \mathfrak{p}^{e_i} \, d\boldsymbol{r} - \int_{\mathcal{M}_i} \tilde{\boldsymbol{n}} \cdot \tilde{\mathfrak{F}}\mathfrak{q}^{e_i}\Big|_{\partial\hat{\mathsf{D}}} \cdot \mathfrak{p}^{e_i} \, d\boldsymbol{r}\right|.
\end{aligned}$$

Note that both terms on the right side of the preceding inequality are of the same type, namely, the error between LGL quadrature integration and exact integration for polynomial of order $2N_{e_i}$. Since $N_{m_i} \geq N_{e_i}$, we need to estimate only the second term. Using an error estimate from [32] together with Stirling's formula we have

$$\begin{aligned}
&\left|\int_{\mathcal{M}_i,N_{e_i}} \tilde{\boldsymbol{n}} \cdot \tilde{\mathfrak{F}}\mathfrak{q}^{e_i}\Big|_{\partial\hat{\mathsf{D}}} \cdot \mathfrak{p}^{e_i} \, d\boldsymbol{r} - \int_{\mathcal{M}_i} \tilde{\boldsymbol{n}} \cdot \tilde{\mathfrak{F}}\mathfrak{q}^{e_i}\Big|_{\partial\hat{\mathsf{D}}} \cdot \mathfrak{p}^{e_i} \, d\boldsymbol{r}\right| \\
&\leq C\frac{N_{e_i}+1}{2N_{e_i}+1}\left(\frac{N_{e_i}-1}{N_{e_i}}\right)^{4N_{e_i}-2}\frac{1}{2^{2N_{e_i}}}\max_{\mathsf{D}^{e_i}}|\mathfrak{q}|,
\end{aligned}$$

which shows that the error introduced by having the weak outflow condition (instead of the strong one which has no error) is exponentially decaying with respect to the

solution order N_{e_i}. This is not surprising, since the error is due to quadrature approximation. Compared to the optimal convergence rate with respect to N_{e_i}, i.e., $N_{e_i}^s$ as in Section 7, the error resulting from the weak outflow condition is much smaller.

One can also study the behavior of the error with respect to the element size, i.e. h_e. In particular, a result for affine meshes from [11] shows that

$$\left| \int_{\mathcal{M}_i, N_{e_i}} \tilde{\boldsymbol{n}} \cdot \tilde{\mathfrak{F}} \mathfrak{q}^{e_i} \Big|_{\partial \hat{\mathsf{D}}} \cdot \mathfrak{p}^{e_i} \, d\boldsymbol{r} - \int_{\mathcal{M}_i} \tilde{\boldsymbol{n}} \cdot \tilde{\mathfrak{F}} \mathfrak{q}^{e_i} \Big|_{\partial \hat{\mathsf{D}}} \cdot \mathfrak{p}^{e_i} \, d\boldsymbol{r} \right| \leq C h_e^{N_{e_i}+1/2} \left| \mathfrak{q} \right|_{N_{e_i}-1, \mathsf{D}^e},$$

where $|\cdot|_{N_{e_i}-1,\mathsf{D}^e}$ is the usual semi-Sobolev norm of order $N_{e_i}-1$. This shows that the error decays to zero at the rate $N_{e_i}+1/2$ with respect to h_{e_i}. □

REMARK 1. *By virtue of both h and p estimates above, we see that even though the inexactness of the LGL quadrature violates the strong outflow condition and hence generates additional boundary terms when integration by parts is performed, these terms are negligible. From now on, if LGL quadrature is used, we implicitly absorb the additional error terms arising from the weak outflow condition into constant in the convergence estimate, as in Theorem 4, or simply ignore them.*

7. Convergence rate analysis. The previous sections show that our discrete approximations, both conforming and non-conforming, are stable. Together with consistency, to be shown below, our approximations are convergent by the Lax-Ritchmyer equivalence theorem. The direct consequence is that the solution can grow at most exponentially in time, which is typically for Lax-Ritchmyer type of convergence. This kind of convergence result is interesting for theoretical analysis, but may not be appropriate for accessing the actual convergence rate of a numerical method. Fortunately, Hesthaven and Warburton [13] show that a direct convergence analysis is possible, allowing a much better upper bound on the error estimation. We adapt this type of direct convergence analysis to derive *a priori* error estimation for our non-conforming approximations.

Recall that interpolation introduces truncation and aliasing errors [7, 20], and hence interpolation is generally different from projection, which has only truncation error. For sufficiently smooth functions, however, the aliasing error either is spectrally small [7, 12, 20] or can be made equal to zero [13]. Following [13], we shall make no distinction between interpolation and projection in what remains.

The following conventions are used in this section. We reserve $\mathfrak{q}$ for the unknown exact solution, $\mathcal{I}_{N_e}\mathfrak{q}$ for the projection of $\mathfrak{q}$ on $\mathcal{P}_{N_e}$, and $\mathfrak{q}_{N_e}$ for solution of the discrete form (3.2). In addition, C denotes a generic constant that may have different values in different contexts, $\mathfrak{q}_d$ is defined by $\mathfrak{q}_d|_{\mathsf{D}^e} = \mathfrak{q}_{N_e}$, and finally a dummy variable q lives in different spaces for different inequalities. To begin, we recall the following famous *hp* approximation error [1, 2, 3],

$$\|q - \mathcal{I}_{N_e} q\|_{H^r(\mathsf{D}^e)} \leq C \frac{h_e^{\sigma_e - r}}{N_e^{s-r}} \|q\|_{H^s(\mathsf{D}^e)}, \quad 0 \leq r \leq s \tag{7.1}$$

$$\|q - \mathcal{I}_{N_e} q\|_{\partial\mathsf{D}^e} \leq C \frac{h_e^{\sigma_e - 1/2}}{N_e^{s-1/2}} \|q\|_{H^s(\mathsf{D}^e)}, \quad s > \frac{1}{2} \tag{7.2}$$

with $h_e = diam\,(\mathsf{D}^e)$, $\sigma_e = \min\{N_e + 1, s\}$, and $\|\cdot\|_{H^r(\mathsf{D}^e)}$ denoting the usual Sobolev norm.

For approximation using tensor product LGL quadrature, the following equivalence of the discrete and continuous norm, an extension of the one dimensional version

in [12], is useful in passing from the discrete norm to the continuous one and vice versa: $\forall q \in \mathcal{P}_N$,

$$\|q\|_{\hat{\mathsf{D}}} \leq \|q\|_{\hat{\mathsf{D}},N} \leq \left(2+\frac{1}{N}\right)^{3/2} \|q\|_{\hat{\mathsf{D}}}\,,$$
$$\|q\|_{\partial\hat{\mathsf{D}}} \leq \|q\|_{\partial\hat{\mathsf{D}},N} \leq \left(2+\frac{1}{N}\right) \|q\|_{\partial\hat{\mathsf{D}}}\,.$$

We first derive the convergence rate for conforming meshes. Since the electromagnetic wave equation and the elastic–acoustic coupling wave equation are similar, we analyze the former and leave out the details of the latter. Denote $T^{\mathfrak{q}} = \left[T^{\boldsymbol{E}}, T^{\boldsymbol{H}}\right]^T$ as the the truncation error that results from substituting the exact solution $\mathfrak{q}$ to the discrete equation (3.2). Using the fact that $\mathfrak{q}$ satisfies the Maxwell's equation, we have

$$\begin{aligned}
\left(\boldsymbol{\ell}_k, \mathcal{I}_{N_e} T^{\boldsymbol{E}}\right)_{\mathsf{D}^e,N_e} &= \left(\boldsymbol{\ell}_k, \mathcal{I}_{N_e}\nabla\times(\boldsymbol{H}-\mathcal{I}_{N_e}\boldsymbol{H})\right)_{\mathsf{D}^e,N_e} \\
&\quad + \left(\boldsymbol{\ell}_k, \frac{1}{2\,\{\{Z\}\}}\boldsymbol{n}\times\left(Z^+\left[\mathcal{I}_{N_e}\boldsymbol{H}\right] - \boldsymbol{n}\times\left[\mathcal{I}_{N_e}\boldsymbol{E}\right]\right)\right)_{\partial\mathsf{D}^e,N_e}, \quad \forall\boldsymbol{\ell}_k \in \mathcal{P}_{N_e} \\
\left(\boldsymbol{\ell}_k, \mathcal{I}_{N_e} T^{\boldsymbol{H}}\right)_{\mathsf{D}^e,N_e} &= \left(\boldsymbol{\ell}_k, \mathcal{I}_{N_e}\nabla\times(\boldsymbol{E}-\mathcal{I}_{N_e}\boldsymbol{E})\right)_{\mathsf{D}^e,N_e} \\
&\quad + \left(\boldsymbol{\ell}_k, \frac{1}{2\,\{\{Y\}\}}\boldsymbol{n}\times\left(Y^+\left[\mathcal{I}_{N_e}\boldsymbol{E}\right] + \boldsymbol{n}\times\left[\mathcal{I}_{N_e}\boldsymbol{H}\right]\right)\right)_{\partial\mathsf{D}^e,N_e}, \quad \forall\boldsymbol{\ell}_k \in \mathcal{P}_{N_e}
\end{aligned}$$

where μ and ε are assumed to be constant on each element D^e, and the mesh is affine. Note that the truncation errors for the electric and magnetic equations are similar, we only need to estimate the former and infer the later. Since $\mathcal{I}_{N_e}T^{\boldsymbol{E}} \in \mathcal{P}_{N_e}$, we can take $\boldsymbol{\ell}_k = \mathcal{I}_{N_e}T^{\boldsymbol{E}}$ and use the Cauchy-Schwarz inequality together with the equivalence of discrete and continuous norms to obtain

$$\begin{aligned}
\left\|\mathcal{I}_{N_e}T^{\boldsymbol{E}}\right\|^2_{\mathsf{D}^e,N_e} &\leq 27^2\left\|\mathcal{I}_{N_e}\nabla\times(\boldsymbol{H}-\mathcal{I}_{N_e}\boldsymbol{H})\right\|_{\mathsf{D}^e}\left\|\mathcal{I}_{N_e}T^{\boldsymbol{E}}\right\|_{\mathsf{D}^e} \\
&\quad + 9^2\left\|\frac{1}{2\,\{\{Z\}\}}\boldsymbol{n}\times\left(Z^+\left[\mathcal{I}_{N_e}\boldsymbol{H}\right] - \boldsymbol{n}\times\left[\mathcal{I}_{N_e}\boldsymbol{E}\right]\right)\right\|_{\partial\mathsf{D}^e}\left\|\mathcal{I}_{N_e}T^{\boldsymbol{E}}\right\|_{\partial\mathsf{D}^e}.
\end{aligned}$$

Now use the following inverse trace inequality [28], $\forall q \in \mathcal{P}_{N_e}$,

$$\|q\|_{\partial\mathsf{D}^e} \leq C\frac{N_e}{h_e^{1/2}}\|q\|_{\mathsf{D}^e} \tag{7.3}$$

to have

$$\begin{aligned}
\left\|\mathcal{I}_{N_e}T^{\boldsymbol{E}}\right\|_{\mathsf{D}^e,N_e} &\leq C\left\|\mathcal{I}_{N_e}\nabla\times(\boldsymbol{H}-\mathcal{I}_{N_e}\boldsymbol{H})\right\|_{\mathsf{D}^e} \\
&\quad + C\frac{N_e}{h_e^{1/2}}\left\|\frac{1}{2\,\{\{Z\}\}}\left(Z^+\left[\mathcal{I}_{N_e}\boldsymbol{H}_\tau\right] - \left[\mathcal{I}_{N_e}\boldsymbol{E}_\tau\right]\right)\right\|_{\partial\mathsf{D}^e},
\end{aligned} \tag{7.4}$$

where we have introduced the tangent components of $\boldsymbol{E}$ and $\boldsymbol{H}$ as

$$\boldsymbol{E}_\tau = \boldsymbol{n}\times(\boldsymbol{n}\times\boldsymbol{E}), \quad \boldsymbol{H}_\tau = \boldsymbol{n}\times\boldsymbol{H}.$$

We now have the following result for the consistency.

LEMMA 1. *Suppose that each component* $\mathfrak{q}_i^e \in H^s(\mathsf{D}^e), s \geq 3/2$, *for* $i = 1,\ldots,d$, *with* $d = 6$ *for electromagnetic case and* $d = 12$ *for elastic–acoustic case. There exists*

a constant C dependent on s, angle condition of D^e, and local values of μ and ε (λ and μ for elastic–acoustic case), but independent of $\mathfrak{q}, h_e$, and N_e such that

$$\|\mathcal{I}_{N_e} T^{\mathfrak{q}}\|_{\mathcal{D}^{N_{el}},d} \leq C \sum_e \frac{h_e^{\sigma_e - 1}}{N_e^{s-3/2}} \|\mathfrak{q}\|_{[H^s(\mathsf{D}^e)]^d} .$$

Proof. Since the proofs for both electromagnetic and elastic–acoustic cases are similar, we provide only the proof for the former. We begin by estimating the bound for the first term on the right side of (7.4). Using approximation result (7.1) we have

$$\|\mathcal{I}_{N_e} \nabla \times (\boldsymbol{H} - \mathcal{I}_{N_e} \boldsymbol{H})\|_{\mathsf{D}^e} \leq \|\nabla \times (\boldsymbol{H} - \mathcal{I}_{N_e} \boldsymbol{H})\|_{\mathsf{D}^e} \leq C \frac{h_e^{\sigma_e - 1}}{N_e^{s-1}} \|\boldsymbol{H}\|_{[H^s(\mathsf{D}^e)]^3} .$$

To estimate the second term we use the regularity of the exact solution, i.e. the tangent component of the field is continuous, and the triangle inequality to bound $\|[\mathcal{I}_{N_e} \boldsymbol{H}_\tau]\|_{\partial \mathsf{D}^e}$, and hence similarly for $\|[\mathcal{I}_{N_e} \boldsymbol{E}_\tau]\|_{\partial \mathsf{D}^e}$, as

$$\|[\mathcal{I}_{N_e} \boldsymbol{H}_\tau]\|_{\partial \mathsf{D}^e} \leq \left\|\boldsymbol{H}_\tau^- - \mathcal{I}_{N_e} \boldsymbol{H}_\tau^-\right\|_{\partial \mathsf{D}^e} + \left\|\boldsymbol{H}_\tau^+ - \mathcal{I}_{N_e} \boldsymbol{H}_\tau^+\right\|_{\partial \mathsf{D}^e}$$

Two terms of the right side of the preceding inequality are of the same type, therefore we need to estimate only the bound for the first term. But this is ready by using (7.2), i.e.,

$$\left\|\boldsymbol{H}_\tau^- - \mathcal{I}_{N_e} \boldsymbol{H}_\tau^-\right\|_{\partial \mathsf{D}^e} \leq C \frac{h_e^{\sigma_e - 1/2}}{N_e^{s-1/2}} \|\boldsymbol{H}_\tau\|_{[H^s(\mathsf{D}^e)]^3} \leq C \frac{h_e^{\sigma_e - 1/2}}{N_e^{s-1/2}} \|\boldsymbol{H}\|_{[H^s(\mathsf{D}^e)]^3} .$$

Now combining the above estimates for both terms on the right hand side of (7.4), summing over all elements and using the discrete Hölder inequality complete the proof. □

REMARK 2. *Note that the proof of Lemma 1 is done for conforming meshes. The proof for non-conforming meshes is almost identical except for bounding the boundary terms which are now defined on the mortars instead on the contributing element faces. But the fields on the mortars are the L^2 orthogonal projections of those on the contributing element faces, which implies L^2 norms of fields on mortars to be at most those on contributing element faces. This shows that the proof for conforming meshes is sufficient.*

We now state the convergence result.

THEOREM 4. *Assume $\mathfrak{q}^e \in [H^s(\mathsf{D}^e)]^d, s \geq 3/2$ with $d = 6$ for electromagnetic case and $d = 12$ for elastic–acoustic case. In addition, suppose $\mathfrak{q}_d(0) = \Pi \mathfrak{q}(0)$. Then, the solution $\mathfrak{q}_d$ of the discrete form (3.2) converges to the exact solution $\mathfrak{q}$, i.e., there exists a constant C that depends only on the angle condition of D^e, s, and the material constants μ and ε (λ and μ for elastic–acoustic case) such that*

$$\|\mathfrak{q}(t) - \mathfrak{q}_d(t)\|_{\mathcal{D}^{N_{el}},d} \leq C \sum_e \left[\frac{h_e^{\sigma_e}}{N_e^s} \|\mathfrak{q}(t)\|_{[H^s(\mathsf{D}^e)]^d} + t \frac{h_e^{\sigma_e - 1}}{N_e^{s-3/2}} \max_{[0,t]} \|\mathfrak{q}(t)\|_{[H^s(\mathsf{D}^e)]^d} \right]$$

Proof. We begin the proof with the following identities

$$\begin{aligned}
&\left(\mathcal{I}_{N_e}\boldsymbol{E}-\boldsymbol{E}_{N_e},\mathcal{I}_{N_e}T^{\boldsymbol{E}}\right)_{\mathsf{D}^e,N_e}=\left(\mathcal{I}_{N_e}\boldsymbol{E}-\boldsymbol{E}_{N_e},\varepsilon\frac{\partial\left(\mathcal{I}_{N_e}\boldsymbol{E}-\boldsymbol{E}_{N_e}\right)}{\partial t}\right)_{\mathsf{D}^e,N_e}\\
&-\left(\mathcal{I}_{N_e}\boldsymbol{E}-\boldsymbol{E}_{N_e},\mathcal{I}_{N_e}\nabla\times\left(\mathcal{I}_{N_e}\boldsymbol{H}-\boldsymbol{H}_{N_e}\right)\right)_{\mathsf{D}^e,N_e}\\
&+\left(\mathcal{I}_{N_e}\boldsymbol{E}-\boldsymbol{E}_{N_e},\frac{1}{2\left\{\{Z\}\right\}}\boldsymbol{n}\times\left(Z^+\left[\mathcal{I}_{N_e}\boldsymbol{H}-\boldsymbol{H}_{N_e}\right]-\boldsymbol{n}\times\left[\mathcal{I}_{N_e}\boldsymbol{E}-\boldsymbol{E}_{N_e}\right]\right)\right)_{\partial\mathsf{D}^e,N_e},\\
&\left(\mathcal{I}_{N_e}\boldsymbol{H}-\boldsymbol{H}_{N_e},\mathcal{I}_{N_e}T^{\boldsymbol{H}}\right)_{\mathsf{D}^e,N_e}=\left(\mathcal{I}_{N_e}\boldsymbol{H}-\boldsymbol{H}_{N_e},\mu\frac{\partial\left(\mathcal{I}_{N_e}\boldsymbol{H}-\boldsymbol{H}_{N_e}\right)}{\partial t}\right)_{\mathsf{D}^e,N_e}\\
&+\left(\mathcal{I}_{N_e}\boldsymbol{H}-\boldsymbol{H}_{N_e},\mathcal{I}_{N_e}\nabla\times\left(\mathcal{I}_{N_e}\boldsymbol{E}-\boldsymbol{E}_{N_e}\right)\right)_{\mathsf{D}^e,N_e}\\
&-\left(\mathcal{I}_{N_e}\boldsymbol{H}-\boldsymbol{H}_{N_e},\frac{1}{2\left\{\{Y\}\right\}}\boldsymbol{n}\times\left(Y^+\left[\mathcal{I}_{N_e}\boldsymbol{E}-\boldsymbol{E}_{N_e}\right]+\boldsymbol{n}\times\left[\mathcal{I}_{N_e}\boldsymbol{H}-\boldsymbol{H}_{N_e}\right]\right)\right)_{\partial\mathsf{D}^e,N_e},
\end{aligned}$$

where we have substituted the exact solution into the discrete equation (3.2), and used $\mathcal{I}_{N_e}\boldsymbol{E}-\boldsymbol{E}_{N_e}$ and $\mathcal{I}_{N_e}\boldsymbol{H}-\boldsymbol{H}_{N_e}$ as test functions for the electric and magnetic equations, respectively.

Following the proof of Theorem 2, we integrate the preceding equations by parts, sum up the resulting equations, cancel the volume terms involving the fluxes, and use the non-positiveness of the boundary integrals to arrive at

$$\frac{1}{2}\frac{d}{dt}\left\|\Pi\mathfrak{q}-\mathfrak{q}_d\right\|^2_{\mathcal{D}^{N_{\mathrm{el}}},d}\leq C\sum_e\left(\mathcal{I}_{N_e}\mathfrak{q}-\mathfrak{q}_{Ne},\mathcal{I}_{N_e}T^{\mathfrak{q}}\right)_{\mathsf{D}^e,N_e},$$

where we have used the fact that the material constants μ and ε are bounded away from zero. Next, we use Cauchy-Schwarz and then the discrete Hölder inequalities, then apply the consistency result of Lemma 1 to obtain

$$\frac{d}{dt}\left\|\Pi\mathfrak{q}-\mathfrak{q}_d\right\|_{\mathcal{D}^{N_{\mathrm{el}}},d}\leq C\sum_e\frac{h_e^{\sigma_e-1}}{N_e^{s-3/2}}\left\|\mathfrak{q}\right\|_{[H^s(\mathsf{D}^e)]^d}\leq C\sum_e\frac{h_e^{\sigma_e-1}}{N_e^{s-3/2}}\max_{[0,t]}\left\|\mathfrak{q}\right\|_{[H^s(\mathsf{D}^e)]^d}$$

which, after integrating in time, yields

$$\left\|\Pi\mathfrak{q}\left(t\right)-\mathfrak{q}_d\left(t\right)\right\|_{\mathcal{D}^{N_{\mathrm{el}}},d}\leq Ct\sum_e\frac{h_e^{\sigma_e-1}}{N_e^{s-3/2}}\max_{[0,t]}\left\|\mathfrak{q}\left(t\right)\right\|_{[H^s(\mathsf{D}^e)]^d},$$

where we have used $\mathfrak{q}_d(0)=\Pi\mathfrak{q}(0)$. Now, using triangle inequality we have,

$$\left\|\mathfrak{q}\left(t\right)-\mathfrak{q}_d\left(t\right)\right\|_{\mathcal{D}^{N_{\mathrm{el}}},d}\leq\left\|\mathfrak{q}\left(t\right)-\Pi\mathfrak{q}\left(t\right)\right\|_{\mathcal{D}^{N_{\mathrm{el}}},d}+\left\|\Pi\mathfrak{q}\left(t\right)-\mathfrak{q}_d\left(t\right)\right\|_{\mathcal{D}^{N_{\mathrm{el}}},d}.$$

Finally, the equivalence of the discrete and continuous norms, and (7.1) ends the proof. □

Remark 3.

Since all norms are equivalent in finite dimensional spaces, the result of Theorem 4 holds for other norms as well, with possibly different constant C. In particular, we have

$$\sum_e\left\|\mathfrak{q}\left(t\right)-\mathfrak{q}_d\left(t\right)\right\|_{\mathsf{D}^e,N_e}\leq C\sum_e\left[\frac{h_e^{\sigma_e}}{N_e^s}\left\|\mathfrak{q}\left(t\right)\right\|_{[H^s(\mathsf{D}^e)]^d}+t\frac{h_e^{\sigma_e-1}}{N_e^{s-3/2}}\max_{[0,t]}\left\|\mathfrak{q}\left(t\right)\right\|_{[H^s(\mathsf{D}^e)]^d}\right]$$

REMARK 4. *We again emphasize that the LGL quadrature introduces additional error terms when the discrete integration by parts is performed. However, they are shown to be negligible in Theorem 2 and Remark 1, hence their absence in the proof of Theorem 4 is justified.*

REMARK 5. *The proof for the LG quadrature follows exactly the same lines and hence is omitted here. The only difference is that all the numerical integrations are exact, and therefore there is no need to invoke the equivalence of discrete and continuous norms.*

REMARK 6. *We have restricted ourselves to the case of affine hexahedral meshes. This enables us to eliminate the volume integrals of fluxes on the right side of equation* (4.1) *since differentiation and interpolation commute. The discrete stability is then ready due to the non-positiveness of the surface integrals of fluxes. Most of the results still hold for meshes with* $J\boldsymbol{a}^i =$ *constant, for* $i = 1, 2, 3$. *In addition, it is not hard to see that all the stability, and hence convergence, results for both conforming and non-conforming approximations are still valid for meshes with curved elements provided that the contravariant fluxes are polynomials with order at most* N^e, *i.e.,*

$$\tilde{\mathfrak{F}}^i = J^e \boldsymbol{a}^i \cdot \mathfrak{F} \in \mathcal{P}_{N^e}, \quad i = 1, 2, 3, \tag{7.5}$$

for which we again have the commutativity of differentiation and interpolation. Together with the metric identities in [19], we again can eliminate the volume integrals after integrating by parts. Moreover, it is clear that our results remain true for other types of meshes, e.g. affine tetrahedral mesh as well, as long as the discrete integration by parts is possible and the commutativity of differentiation and interpolation is valid. For general curvilinear hexahedral meshes, it is not clear whether the volume integrals vanish (or negative) or not since differentiation and interpolation generally do not commute (even over-integration is not helpful in this case).

8. Numerical results. In this section, we present numerical results to support our theoretical findings in the previous sections. For simplicity, we consider only h-non-conforming meshes, for which we can use the DGSEM code described in [33] as a starting point. For elastic–acoustic wave equations, extensive numerical results in Wilcox *et al.* [33] can be used to validate our stability and convergence rate. They numerically show that the L^2 error decays exponentially for cases with analytic exact solution (which can be justified by the work of Houston *et al.* [15]). For other cases, most of their numerical results show optimal convergence rate of $N + 1$ (recall that our paper uses N in place of p for polynomial orders), except for one case with rate $N+1/2$. This is typical, since the sharp rate $N+1/2$ happens only for some particular meshes as shown in [25], while the optimal convergence rate is observed for most of other meshes. Note that our convergence rate result seems to be suboptimal in both h and N, as shown in Theorem 4. In particular, we loose one-half order in h and one order in N. This loss is incurred from estimating the truncation error and using the inverse trace inequality (7.3), and we do not yet find a different proof to obtain the optimal convergence rate both in h and N. Therefore, it is not clear to us whether our convergence result is sharp or suboptimal.

Our Maxwell's code is built on top of the code of Wilcox *et al.* [33]. The scalability of the DGSEM code is clearly demonstrated in their paper for elastic–acoustic waves up to 220,000 cores, and we will not repeat it here for the Maxwell's equations. Instead, we concentrate on validating our convergence results for the electromagnetic wave case. For h-non-conforming meshes, the result in Theorem 4 can be simplified

388 to

$$\|\mathfrak{q}(t) - \mathfrak{q}_d(t)\|_{\mathcal{D}^{N_{\mathrm{el}},d}} \leq Ct \frac{h^{\sigma-1}}{N^{s-3/2}} \max_{[0,t],e} \|\mathfrak{q}(t)\|_{[H^s(\mathsf{D}^e)]^d}, \tag{8.1}$$

389 where N is the solution order, $h = \max_e h_e$, and $\sigma = \min\{N+1, s\}$.

390 Explicit time integration and method for choosing the Courant-Friedrichs-Lewy
391 (CFL) number are similar to those in [33]. Recall that our analysis is for exact time
392 integration, that is, the convergence rate only accounts for the spatial discretization
393 error due to DGSEM. As a result, in order to accurately validate our convergence rate
394 analysis, we need to make the time discretization error negligible.

The first example considered is a Snell's law in which a perpendicular polarized uniform plane wave is incident at an oblique angle on the reflecting interface $z = 0$ between two regions with properties (μ_1, ε_1) and (μ_2, ε_2), respectively, as shown in Figure 8.1. The incident electric field $\boldsymbol{E}^i_\perp$ is oriented perpendicularly to the plane of

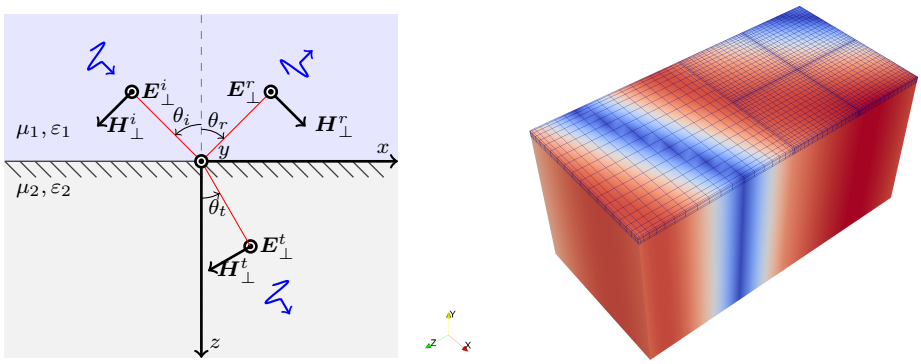

(a) (b)

FIG. 8.1. *Snell's law example: 8.1(a) Geometry setting; 8.1(b) Magnitude of the initial electric field, $\|\boldsymbol{E}\|$, plotted on the coarsest mesh of the Snell example with solution order of $N = 20$. Also shown are the LGL points on a portion of the mesh.*

incident xz. This example is therefore a two-dimensional phenomenon. The general form of the exact solution for this class of problems can be found in [4]. Here we consider the following exact solution for the incident wave,

$$\begin{aligned}
\boldsymbol{E}^i_{\perp y} &= E_o \cos\left[\omega t - \beta_1 \left(x \sin\theta_i + z \cos\theta_i\right)\right], \\
\boldsymbol{H}^i_{\perp x} &= -\frac{E_o}{\eta_1} \cos\theta_i \cos\left[\omega t - \beta_1 \left(x \sin\theta_i + z \cos\theta_i\right)\right], \\
\boldsymbol{H}^i_{\perp z} &= \frac{E_o}{\eta_1} \sin\theta_i \cos\left[\omega t - \beta_1 \left(x \sin\theta_i + z \cos\theta_i\right)\right], \\
\boldsymbol{E}^i_{\perp x} &= \boldsymbol{E}^i_{\perp z} = \boldsymbol{H}^i_{\perp y} = 0,
\end{aligned}$$

395 with

$$\beta_1 = \omega\sqrt{\mu_1 \varepsilon_1}, \quad \eta_1 = \sqrt{\frac{\mu_1}{\varepsilon_1}}.$$

The corresponding exact solution for the reflected wave is given by,

$$\begin{aligned}
\boldsymbol{E}^r_{\perp y} &= \Gamma^b E_o \cos\left[\omega t - \beta_1 \left(x \sin\theta_r - z\cos\theta_r\right)\right], \\
\boldsymbol{H}^r_{\perp x} &= \Gamma^b \frac{E_o}{\eta_1} \cos\theta_r \cos\left[\omega t - \beta_1 \left(x \sin\theta_r - z\cos\theta_r\right)\right], \\
\boldsymbol{H}^r_{\perp z} &= \Gamma^b \frac{E_o}{\eta_1} \sin\theta_r \cos\left[\omega t - \beta_1 \left(x \sin\theta_r - z\cos\theta_r\right)\right], \\
\boldsymbol{E}^r_{\perp x} &= \boldsymbol{E}^r_{\perp z} = \boldsymbol{H}^r_{\perp y} = 0,
\end{aligned}$$

and for the transmitted wave by,

$$\begin{aligned}
\boldsymbol{E}^t_{\perp y} &= T^b E_o \cos\left[\omega t - \beta_2 \left(x \sin\theta_t + z\cos\theta_t\right)\right], \\
\boldsymbol{H}^t_{\perp x} &= -T^b \frac{E_o}{\eta_2} \cos\theta_t \cos\left[\omega t - \beta_2 \left(x \sin\theta_t + z\cos\theta_t\right)\right], \\
\boldsymbol{H}^t_{\perp z} &= T^b \frac{E_o}{\eta_2} \sin\theta_t \cos\left[\omega t - \beta_1 \left(x \sin\theta_t + z\cos\theta_t\right)\right], \\
\boldsymbol{E}^t_{\perp x} &= \boldsymbol{E}^t_{\perp z} = \boldsymbol{H}^t_{\perp y} = 0,
\end{aligned}$$

where

$$\beta_2 = \omega\sqrt{\mu_2\varepsilon_2}, \quad \eta_2 = \sqrt{\frac{\mu_2}{\varepsilon_2}}, \quad \theta_r = \theta_i, \quad \beta_2 \sin\theta_t = \beta_1 \sin\theta_i,$$

$$\Gamma^b = \frac{\eta_2\cos\theta_i - \eta_1\cos\theta_t}{\eta_2\cos\theta_i + \eta_1\cos\theta_t}, \quad T^b = \frac{2\eta_2\cos\theta_i}{\eta_2\cos\theta_i + \eta_1\cos\theta_t}.$$

For our numerical example, we choose,

$$\omega = 2\pi, \quad \mu_1 = 1, \quad \mu_2 = 2, \quad \varepsilon_1 = 1, \quad \varepsilon_2 = 2, \quad E_o = 1, \quad \theta_i = \pi/4,$$

and the box $[-\frac{1}{8}, \frac{1}{8}] \times [-\frac{1}{8}, \frac{1}{8}] \times [-\frac{1}{4}, \frac{1}{4}]$ as the computational domain. For the purpose of validating our convergence analysis on non-conforming meshes, we always refine the incident region (μ_1, ε_1) one level further than the transmitted region (μ_2, ε_2). Therefore, all non-conforming faces reside on the reflecting interface $z = 0$. In Figure 8.1(b), we show the magnitude of the initial electric field on the coarsest mesh consisting of one element in the transmitted region and eight elements in the incident region. Also shown are the LGL points on a portion of the mesh with solution order $N = 20$. The exact solution is prescribed at faces of the box as boundary conditions to mimic the unbounded domain. For this example, the mesh consists of only parallelepipeds, i.e., it is affine, and hence our analytical results, in particular stability and convergence, hold.

In order to find a suitable CFL number to obtain negligible time discretization error, we plot the error in the L^2-norm versus the CFL number for $N = 5$ and $h = 0.1$. Unnoticeable change of the error for $CFL < 0.2$ in Figure 8.2 suggests that we should choose $CFL = 0.1$. Using a similar study on the error in the L^2-norm versus the CFL number for the other examples, we observe that $CFL = 0.1$ seems to lead to negligibly small discretization error for all examples considered in this paper.

Figure 8.3(a) shows the L^2-norm error, i.e. $\|\mathfrak{q} - \mathfrak{q}_d\|_{\mathcal{D}^{N_{\text{el}}},d}$, at $t = 1$ versus the mesh size h for various solution orders N. In order to compute the order of convergence, we fit–using the usual least square method–the error-versus-h curves with

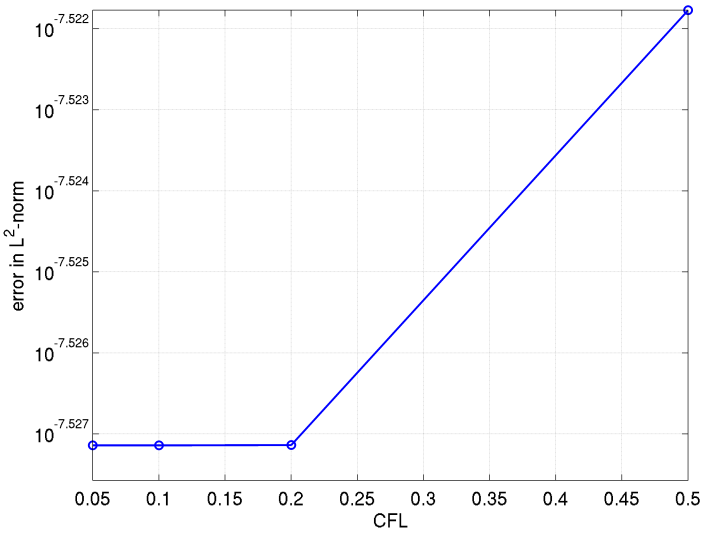

FIG. 8.2. *Snell's law example: Error in the L^2-norm versus the CFL number for the Snell law example with $N = 5$ and $h = 0.1$.*

straight lines whose slopes are used as convergence rates. As can be seen, the DGSEM delivers optimal h-convergence rate of $N + 1$, which is typical for DG methods, even though the sharp rate is $N + 1/2$. Again, our above analytical result is suboptimal by $1/2$ compared to the sharp rate, and by 1 compared to the observed rate. We also plot the L^2-norm error as a function of the solution order N in Figure 8.3(b) in linear-log scale with various mesh sizes h. The result shows that the convergence is exponential, which is not surprising since our exact solution is element-wise analytic. This can be proved rigorously by an argument in [16] for quadrilateral (and hence hexahedral) meshes. This result confirms that if the mesh is aligned with the discontinuous interfaces, DG methods are capable of delivering optimal convergence rate in h, and the convergence in N is exponential if the exact solution is element-wise analytic.

We next verify the linear growing rate in time of the L^2-norm error in Figure 8.4. We run simulations with $h = 0.22$ up to $t = 100$ for solution order N from 1 to 5. As can be seen, the errors steadily oscillate but do not seem to grows in time. Our estimate (8.1) seems to be conservative in this case. However, the next example shows that it is indeed a sharp result.

In the second numerical example, we consider a partially filled rectangular waveguide shown in Figure 8.5. This is a longitudinal section electric in y-direction. The properties of the dielectric and free space regions are given by (μ_d, ε_d) and (μ_o, ε_o), respectively. Unlike the first example, this example is a three-dimensional phenomenon. Again, one can find a general solution in [4]. Here, we consider the following exact

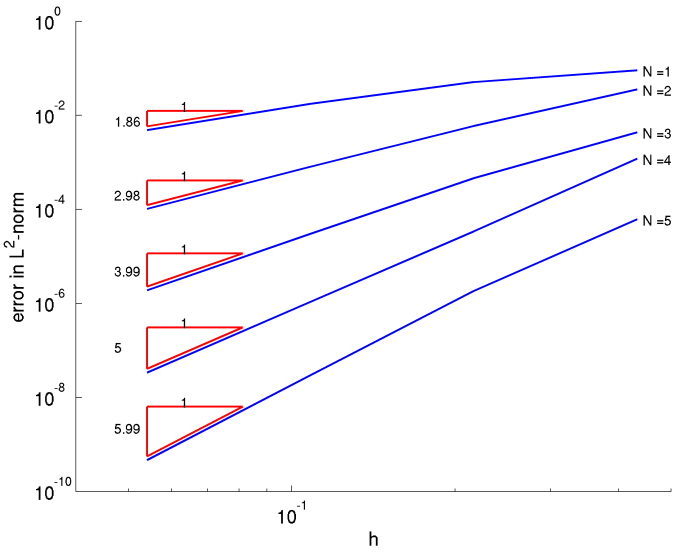

(a)

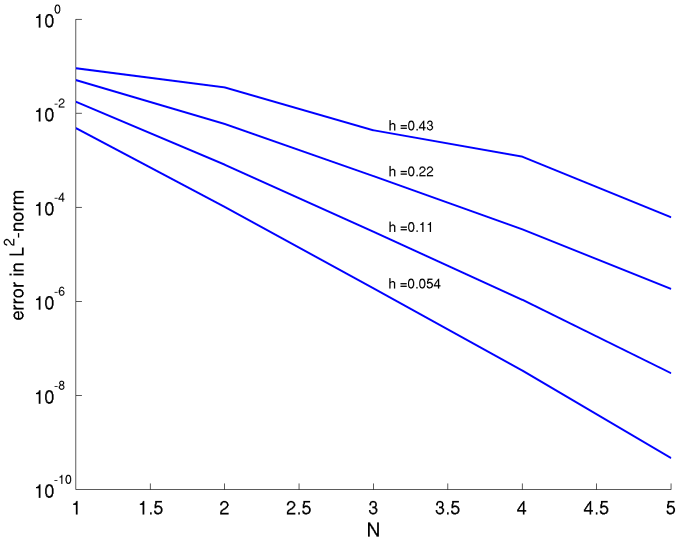

(b)

FIG. 8.3. *Snell's law example: 8.3(a) Plot of the error in L^2-norm, i.e. $\|\mathfrak{q} - \mathfrak{q}_d\|_{\mathcal{D}^{N_{el},d}}$, at time $t = 1$ as the mesh is refined in h with solution order from $N = 1$ to $N = 5$; 8.3(b) Plot of the error in L^2-norm, i.e. $\|\mathfrak{q} - \mathfrak{q}_d\|_{\mathcal{D}^{N_{el},d}}$, at time $t = 1$ as the mesh is refined in N. The convergence is shown for four different mesh sizes $h = \{0.43, 0.22, 0.11, 0.054\}$.*

traveling wave solution in the free space domain,

$$
\begin{aligned}
\boldsymbol{E}_{x_o} &= A_o \frac{\beta_z}{\varepsilon_o} \cos(\beta_{x_o} x) \sin[\beta_{y_o}(b-y)] \sin(\omega t - \beta_z z), \\
\boldsymbol{E}_{y_o} &= 0, \\
\boldsymbol{E}_{z_o} &= A_o \frac{\beta_{x_o}}{\varepsilon_o} \sin(\beta_{x_o} x) \sin[\beta_{y_o}(b-y)] \cos(\omega t - \beta_z z), \\
\boldsymbol{H}_{x_o} &= A_o \frac{\beta_{x_o}\beta_{y_o}}{\omega\mu_o\varepsilon_o} \sin(\beta_{x_o} x) \cos[\beta_{y_o}(b-y)] \sin(\omega t - \beta_z z), \\
\boldsymbol{H}_{y_o} &= A_o \frac{\left(\beta_{x_o}^2 + \beta_z^2\right)}{\omega\mu_o\varepsilon_o} \cos(\beta_{x_o} x) \sin[\beta_{y_o}(b-y)] \sin(\omega t - \beta_z z), \\
\boldsymbol{H}_{z_o} &= A_o \frac{\beta_z\beta_{y_o}}{\omega\mu_o\varepsilon_o} \cos(\beta_{x_o} x) \cos[\beta_{y_o}(b-y)] \cos(\omega t - \beta_z z),
\end{aligned}
$$

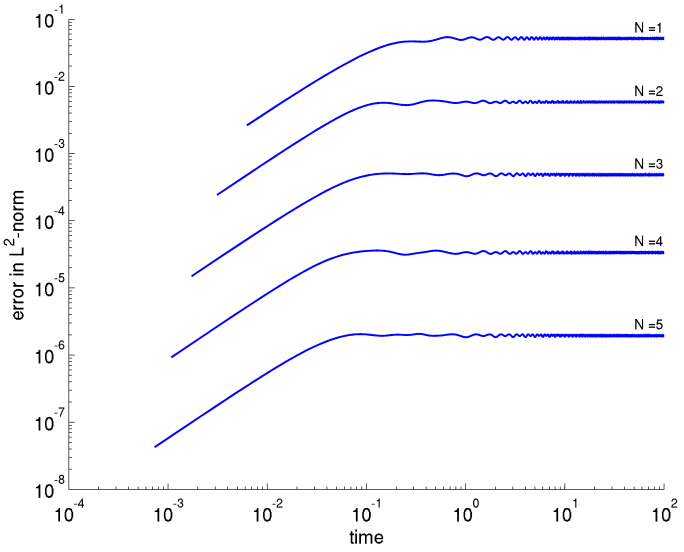

FIG. 8.4. *Snell's law example: Plot of the error in L^2-norm, i.e. $\|\mathfrak{q} - \mathfrak{q}_d\|_{\mathcal{D}^{N_{el},d}}$, up to time $t = 100$ for various solution orders ranging from $N = 1$ to $N = 5$.*

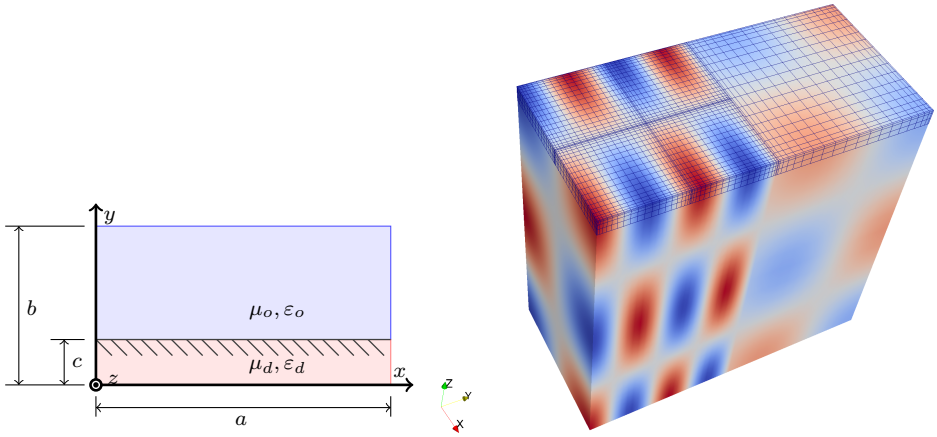

(a) (b)

FIG. 8.5. *Partial filled waveguide example: 8.5(a) Geometry setting; 8.5(b) Magnitude of the initial magnetic field, $\|\boldsymbol{H}\|$, on the coarsest mesh of the partial filled rectangular waveguide example with solution order of $N = 20$. Also shown are the LGL points on a portion of the mesh.*

and the corresponding exact traveling wave solution in the dielectric domain,

$$\begin{aligned}
\boldsymbol{E}_{x_d} &= A_d \frac{\beta_z}{\varepsilon_d} \cos(\beta_{x_d} x) \sin(\beta_{y_d} y) \sin(\omega t - \beta_z z), \\
\boldsymbol{E}_{y_d} &= 0, \\
\boldsymbol{E}_{z_d} &= A_d \frac{\beta_{x_d}}{\varepsilon_d} \sin(\beta_{x_d} x) \sin(\beta_{y_d} y) \cos(\omega t - \beta_z z), \\
\boldsymbol{H}_{x_d} &= -A_d \frac{\beta_{x_d}\beta_{y_d}}{\omega\mu_d\varepsilon_d} \sin(\beta_{x_d} x) \cos(\beta_{y_d} y) \sin(\omega t - \beta_z z), \\
\boldsymbol{H}_{y_d} &= A_d \frac{(\beta_{x_d}^2 + \beta_z^2)}{\omega\mu_d\varepsilon_d} \cos(\beta_{x_d} x) \sin(\beta_{y_d} y) \sin(\omega t - \beta_z z), \\
\boldsymbol{H}_{z_d} &= -A_d \frac{\beta_z\beta_{y_d}}{\omega\mu_d\varepsilon_d} \cos(\beta_{x_d} x) \cos(\beta_{y_d} y) \cos(\omega t - \beta_z z),
\end{aligned}$$

where the following relations hold,

$$\begin{aligned}
&\beta_{x_o} = \beta_{x_d} = \frac{m\pi}{a}, \quad m = 1, 2, \ldots, \\
&\omega^2 \mu_o \varepsilon_o = \beta_{x_o}^2 + \beta_{y_o}^2 + \beta_z^2, \\
&\omega^2 \mu_d \varepsilon_d = \beta_{x_d}^2 + \beta_{y_d}^2 + \beta_z^2, \\
&\frac{\beta_{y_o}}{\mu_o} A_o \cot\left[\beta_{y_o}(b-c)\right] = -\frac{\beta_{y_d}}{\mu_d} A_d \cot\left(\beta_{y_d} c\right)
\end{aligned}$$

For our numerical example, we choose,

$$\begin{aligned}
&\omega = 6.0541, \quad \sqrt{\frac{\varepsilon_o}{\mu_o}} = 1, \quad \mu_o = 2, \quad \sqrt{\frac{\varepsilon_o}{\mu_o}} = 0.5, \quad \mu_d = 2.2, \\
&\beta_{x_o} = \beta_{x_d} = \beta_z = \pi, \quad A_o = 1, \quad m = 1, \quad c = 1,
\end{aligned}$$

and the box $[0,1] \times [0,2] \times [0,2]$ as the computational domain. For the purpose of validating our convergence analysis on non-conforming meshes, the mesh portion in the dielectric region is always one level finer than that in the free space region. Therefore, all non-conforming faces reside on the interface $y = c$. In Figure 8.5(b), we show the magnitude of the initial magnetic field on the coarsest mesh consisting of one element in the free space region and eight elements in the dielectric region. Also shown are the LGL points on a portion of the mesh with solution order $N = 20$. On the x- and y-surfaces of the box, the PEC boundary condition is applied, while periodic boundary condition is employed on the z-surfaces.

Figure 8.6(a) shows the L^2-norm error, at $t = 1$ versus the mesh size h for various solution orders N. We also plot the L^2-norm error as a function of the solution order N in Figure 8.6(b) with various mesh sizes h. Similar to the first example, we have optimal h-convergence rate of $N + 1$ and exponential N-convergence rate.

Figure 8.7 shows the growth of L^2-norm error in time. We run simulations with $h = 0.61$ up to $t = 100$ for solution order N from 1 to 4. As can be seen, the error grows at most linearly in time which agrees with the analytical estimate (8.1).

In the third example, we consider a cylindrical wave guide with transverse electric mode in the z-direction (TE^z) as shown in Figure 8.8. This is a three dimensional phenomenon whose an exact solution is given by (exact solution with more general form can be found in [4]),

$$\begin{aligned}
\boldsymbol{E}_\rho &= A \frac{m}{\varepsilon \rho} J_m\left(\beta_\rho \rho\right) \sin\left(m\theta\right) \cos\left(\omega t - \beta_z z\right), \\
\boldsymbol{E}_\theta &= A \frac{\beta_\rho}{\varepsilon} J'_m\left(\beta_\rho \rho\right) \cos\left(m\theta\right) \cos\left(\omega t - \beta_z z\right), \\
\boldsymbol{E}_z &= 0, \\
\boldsymbol{H}_\rho &= -A \frac{\beta_z \beta_\rho}{\omega \mu \varepsilon} J'_m\left(\beta_\rho \rho\right) \cos\left(m\theta\right) \cos\left(\omega t - \beta_z z\right), \\
\boldsymbol{H}_\theta &= A \frac{m}{\rho} \frac{\beta_z}{\omega \mu \varepsilon} J_m\left(\beta_\rho \rho\right) \sin\left(m\theta\right) \cos\left(\omega t - \beta_z z\right), \\
\boldsymbol{H}_z &= A \frac{\beta_\rho^2}{\omega \mu \varepsilon} J_m\left(\beta_\rho \rho\right) \cos\left(m\theta\right) \sin\left(\omega t - \beta_z z\right),
\end{aligned}$$

where J_m denotes the mth-order Bessel function of the first kind, and

$$J'_m\left(\beta_\rho \rho\right) = \frac{\partial J_m\left(\beta_\rho \rho\right)}{\partial\left(\beta_\rho \rho\right)}.$$

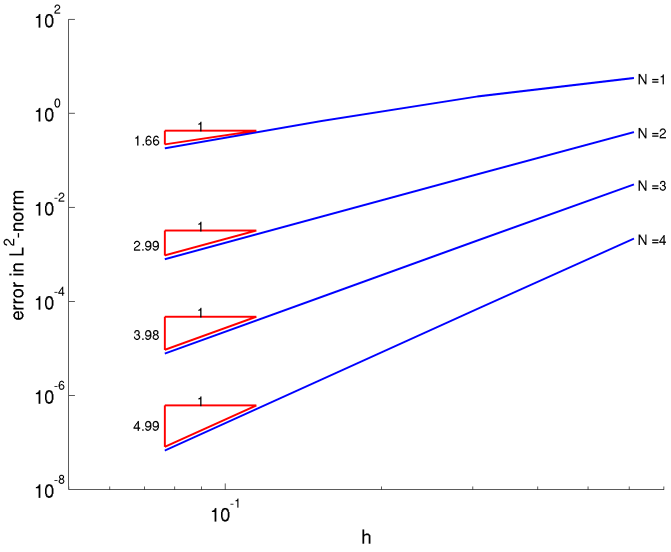

(a)

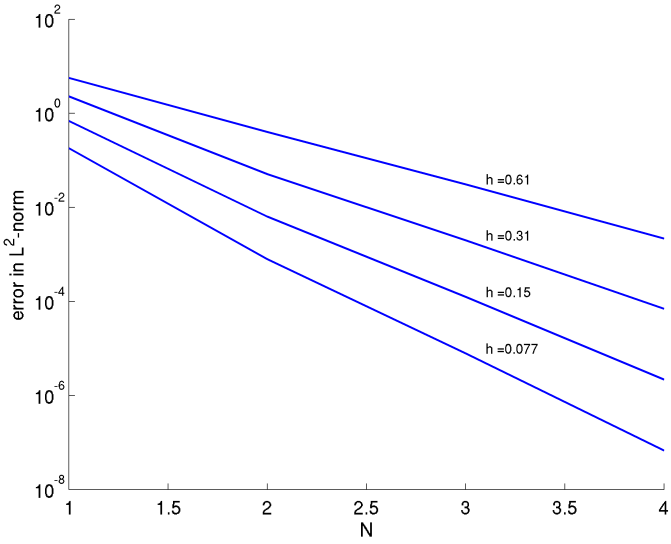

(b)

FIG. 8.6. *Partial filled waveguide example: 8.6(a) Plot of the error in L^2-norm, i.e. $\|\mathfrak{q} - \mathfrak{q}_d\|_{\mathcal{D}^{N_{el}},d}$, at time $t = 1$ as the mesh is refined in h with solution order from $N = 1$ to $N = 4$; 8.6(b) Plot of the error in L^2-norm, i.e. $\|\mathfrak{q} - \mathfrak{q}_d\|_{\mathcal{D}^{N_{el}},d}$, at time $t = 1$ as the mesh is refined in N. The convergence is shown for four different mesh sizes $h = \{0.61, 0.31, 0.15, 0.077\}$.*

452 The relation between β_ρ and β_z is given by

$$\beta_\rho^2 + \beta_z^2 = \omega^2 \mu \varepsilon,$$

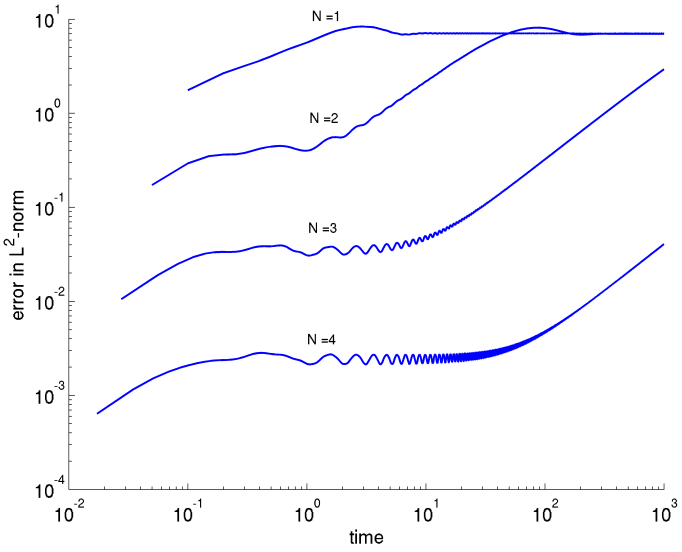

FIG. 8.7. *Partial filled waveguide example: Plot of the error in L^2-norm, i.e. $\|\mathfrak{q} - \mathfrak{q}_d\|_{\mathcal{D}^{N_{el},d}}$, up to time $t = 100$ for various solution orders ranging from $N = 1$ to $N = 4$.*

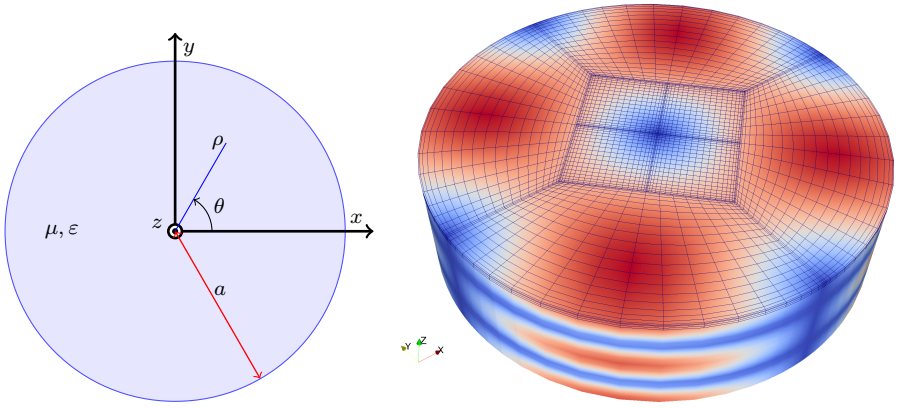

(a) (b)

FIG. 8.8. *Cylindrical waveguide example: 8.8(a) Geometry setting for the transverse electric mode in the z-direction; 8.8(b) Magnitude of the initial electric field, $\|\boldsymbol{E}\|$, plotted on the coarsest mesh of the cylindrical waveguide example with solution order of $N = 20$. Also shown are the LGL points on a portion of the mesh.*

and $\beta_\rho a$ is a zero of J'_m. For our numerical results, we choose

$$a = 2, \quad m = 2, \quad \beta_\rho a = 3.054237, \quad \beta_z = 2\pi, \quad \mu = 1, \quad \epsilon = 0.25, \quad A = 1.5.$$

This is our first example involving curved geometry. For simplicity, we use isoparametric representation for all elements in the mesh. For elements with curved faces, the LGL interpolation points are exactly positioned on the cylindrical surfaces. It is important to point out that the affine assumption is sufficient, but may not be necessary, to obtain stability and convergence analysis. For that reason, it makes sense

for us to try our code on this curved geometry example.

In order to mimic the infinite length in the z-direction, we consider only the portion of cylinder from $z = 0$ to $z = -1$, and supply the exact solution at these two surfaces while applying the PEC condition on the cylindrical surface. Our coarsest mesh consists of one affine hexahedron in the center surrounded by four curved hexahedra. For the purpose of testing the convergence rate on non-conforming meshes with curved geometry, the mesh for the central hexahedron is always one level finer than that of the surrounding hexahedra. In Figure 8.8(b), we show the magnitude of the initial electric field on the coarsest mesh consisting of four surrounding elements and eight elements in the center. Also shown are the LGL points on a portion of the mesh with solution order $N = 20$.

We next numerically study the convergence rate both in h and in N. Figure 8.9(a) shows the L^2-norm error, at $t = 1$ versus the mesh size h for various solution orders N. Figure 8.9(b) plots the L^2-norm error as a function of the solution order N with various mesh sizes h. It can be seen that we again have optimal h-convergence rate of $N + 1$ and exponential N-convergence rate for this non-conforming curved mesh.

In the last three examples, electromagnetic waves travel in unbounded domain in one or more dimensions. In the fourth example, we consider electromagnetic waves trapped in a finite domain with curved boundaries. Probably the most popular example for this kind of problem is the metallic spherical cavity. Figure 8.10 shows the geometry of the problem whose part of the mesh is taken out for clarity. Also shown in Figure 8.10(b) is the magnitude of the initial electric field on a portion of a non-conforming curved mesh.

An exact solution for the spherical cavity in transverse electric mode (TE^r) with radius $r = a$ in the spherical coordinates (r, θ, ϕ) is as follows,

$$
\begin{aligned}
\boldsymbol{E}_r &= 0, \\
\boldsymbol{E}_\theta &= A\frac{m}{\varepsilon r \sin\theta}\hat{J}_n(\beta r) P_n^m(\cos\theta)\sin(m\phi)\cos(\omega t), \\
\boldsymbol{E}_\phi &= -A\frac{\sin\theta}{\varepsilon r}\hat{J}_n(\beta r) P_n^{m'}(\cos\theta)\cos(m\phi)\cos(\omega t), \\
\boldsymbol{H}_r &= A\frac{\beta^2}{\omega\mu\varepsilon}\left(\hat{J}_n(\beta r) + \hat{J}_n''(\beta r)\right) P_n^m(\cos\theta)\cos(m\phi)\sin(\omega t), \\
\boldsymbol{H}_\theta &= -A\frac{\beta\sin\theta}{\omega\mu\varepsilon r}\hat{J}_n'(\beta r) P_n^{m'}(\cos\theta)\cos(m\phi)\sin(\omega t), \\
\boldsymbol{H}_\phi &= -A\frac{m\beta}{\omega\mu\varepsilon r\sin\theta}\hat{J}_n'(\beta r) P_n^m(\cos\theta)\sin(m\phi)\sin(\omega t),
\end{aligned}
$$

where

$$
\beta^2 = \omega^2\mu\varepsilon, \quad P_n^{m'}(\cos\theta) = \frac{\partial P_n^m(\cos\theta)}{\partial(\cos\theta)}, \quad \hat{J}_n(\beta r) = \sqrt{\frac{\pi\beta r}{2}} J_{n+\frac{1}{2}}(\beta r),
$$

with J_n as Bessel functions of the first kind, P_n^m as associated Legendre polynomials, and βa as zeros of spherical Bessel functions of the first kind $\hat{J}_n$. The operator $(\cdot)'$ acting a quantity denotes the derivative with respect to the argument of that quantity, for example, it means derivative with respect to βr for the spherical Bessel functions of the first kind and to $\cos\theta$ for the associated Legendre polynomials.

For our numerical results, we choose,

$$
a = \sqrt{3}, \quad m = 2, \quad n = 3, \quad \mu = 1, \quad \varepsilon = 0.25, \quad A = 1.5, \quad \beta a = 6.9879.
$$

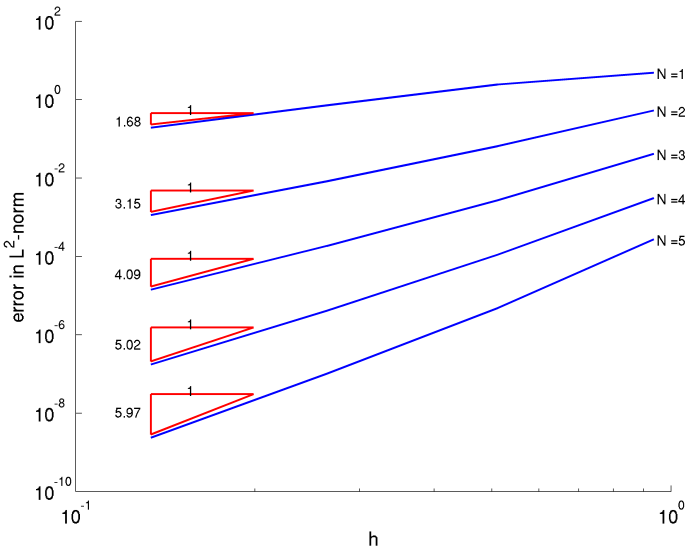

(a)

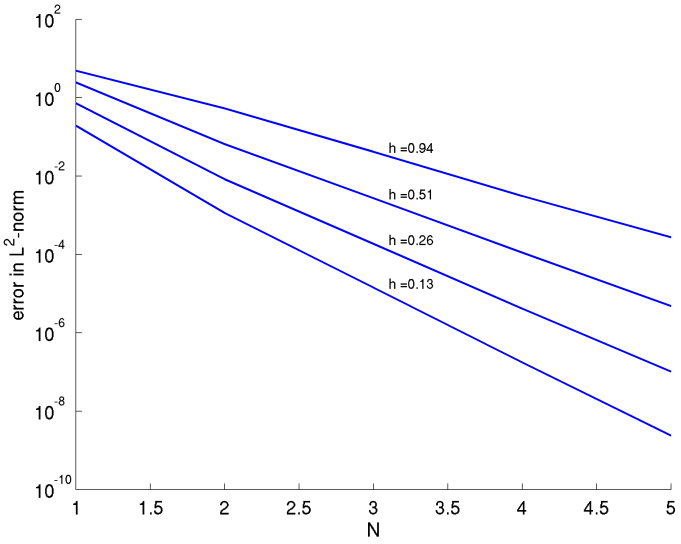

(b)

FIG. 8.9. *Cylindrical waveguide example: 8.9(a) Plot of the error in L^2-norm, i.e. $\|\mathfrak{q} - \mathfrak{q}_d\|_{\mathcal{D}^{N_{el}},d}$, at time $t = 1$ as the mesh is refined in h with solution order from $N = 1$ to $N = 4$; 8.9(b) Plot of the error in L^2-norm, i.e. $\|\mathfrak{q} - \mathfrak{q}_d\|_{\mathcal{D}^{N_{el}},d}$, at time $t = 1$ as the mesh is refined in N. The convergence is shown for four different mesh sizes $h = \{0.94, 0.51, 0.26, 0.13\}$.*

Figure 8.11(a) shows the L^2-norm error, at $t = 0.2$ versus the mesh size h for various solution orders N. Figure 8.11(b) plots the L^2-norm error as a function of the solution order N with various mesh sizes h. It can be seen that we again have optimal h-convergence rate of $N + 1$ and exponential N-convergence rate for this

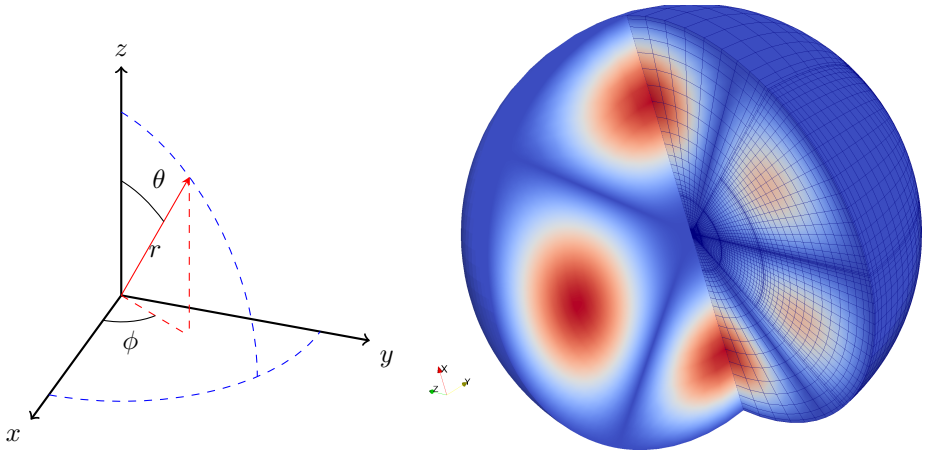

FIG. 8.10. *Spherical cavity example: 8.10(a) Spherical coordinates* (r, θ, ϕ) *for the spherical cavity and spherical obstacle scattering examples; 8.10(b) Magnitude of the initial electric field,* $\|\boldsymbol{E}\|$*, plotted on a part of a non-conforming curved mesh with solution order of* $N = 20$*. Also shown are the LGL points on a portion of the mesh.*

non-conforming curved mesh.

The last example considered in this paper is the scattering of electromagnetic waves from a sphere, where we combine scattering with a non-conforming curved mesh. Physically, the free space region in unbounded, hence we employ a perfectly matched layer (PML) to truncate the domain to make the computation feasible. In particular, the unsplit PML resulting from a modified Berenger model, which is equivalent to the uniaxial model or the Lorentz model [31, 6], is used (see equation (5.12) of [31] for details). For simplicity, we normalize the Maxwell's equation so that the permittivity and permeability of the free space are unity, i.e., $\mu_o = \varepsilon_o = 1$, and discretize the scattered formulation instead of the total field one. Details on normalization and scattered field formulation can be found in [13]. The problem setup can be seen in Figure 8.12, where a is the radius of the sphere, b the distance from the center of the sphere to the interface of the truncated physical domain and the PML domain, and c the distance from the center of the sphere to the end of the PML region. That is, the truncated physical domain is inside the box $[-b, b]^3$ containing the sphere, and the PML region is the complement of the box $[-b, b]^3$ with respect to the box $[-c, c]^3$.

We choose the following incident wave,

$$\boldsymbol{E}^{inc} = e^{j\omega(z-t)}\boldsymbol{e}_1, \quad \boldsymbol{H}^{inc} = e^{j\omega(z-t)}\boldsymbol{e}_2,$$

with $j^2 = -1$. The corresponding exact solutions of the scattered fields in the spherical

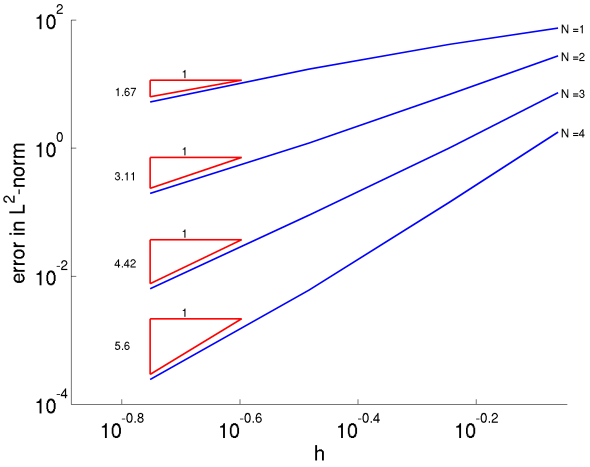

(a)

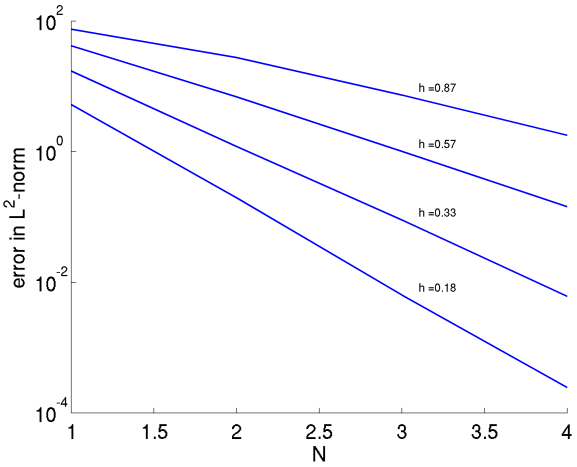

(b)

FIG. 8.11. *Spherical cavity example: 8.11(a) Plot of the error in L^2-norm, i.e. $\|\mathfrak{q} - \mathfrak{q}_d\|_{\mathcal{D}^{N_{el},d}}$, at time $t = 0.2$ as the mesh is refined in h with solution order from $N = 1$ to $N = 4$; 8.11(b) Plot of the error in L^2-norm, i.e. $\|\mathfrak{q} - \mathfrak{q}_d\|_{\mathcal{D}^{N_{el},d}}$, at time $t = 0.2$ as the mesh is refined in N. The convergence is shown for four different mesh sizes $h = \{0.87, 0.57, 0.33, 0.18\}$.*

coordinates (r, θ, ϕ) are given by,

$$\boldsymbol{E}_r = -j\frac{\cos\phi}{(\beta r)^2}\sum_{n=1}^{\infty} n\,(n+1)\,b_n \hat{H}_n^{(1)}(\beta r)\,P_n^1(\cos\theta)\,e^{-\omega t},$$

$$\boldsymbol{E}_\theta = \frac{\cos\phi}{\beta r}\sum_{n=1}^{\infty}\left[a_n \hat{H}_n^{(1)}(\beta r)\,\frac{P_n^1(\cos\theta)}{\sin\theta} + jb_n \hat{H}^{(1)'}(\beta r)\,P_n^{1'}(\cos\theta)\sin\theta\right]e^{-\omega t},$$

$$\boldsymbol{E}_\phi = \frac{\sin\phi}{\beta r}\sum_{n=1}^{\infty}\left[a_n \hat{H}_n^{(1)}(\beta r)\,P_n^{1'}(\cos\theta)\sin\theta + jb_n \hat{H}^{(1)'}(\beta r)\,\frac{P_n^1(\cos\theta)}{\sin\theta}\right]e^{-\omega t},$$

$$\boldsymbol{H}_r = -j\frac{\sin\phi}{(\beta r)^2}\sum_{n=1}^{\infty} n\,(n+1)\,a_n \hat{H}_n^{(1)}(\beta r)\,P_n^1(\cos\theta)\,e^{-\omega t},$$

$$\boldsymbol{H}_\theta = \frac{\sin\phi}{\beta r}\sum_{n=1}^{\infty}\left[b_n \hat{H}_n^{(1)}(\beta r)\,\frac{P_n^1(\cos\theta)}{\sin\theta} + ja_n \hat{H}^{(1)'}(\beta r)\,P_n^{1'}(\cos\theta)\sin\theta\right]e^{-\omega t},$$

$$\boldsymbol{H}_\phi = -\frac{\cos\phi}{\beta r}\sum_{n=1}^{\infty}\left[b_n \hat{H}_n^{(1)}(\beta r)\,P_n^{1'}(\cos\theta)\sin\theta + ja_n \hat{H}^{(1)'}(\beta r)\,\frac{P_n^1(\cos\theta)}{\sin\theta}\right]e^{-\omega t},$$

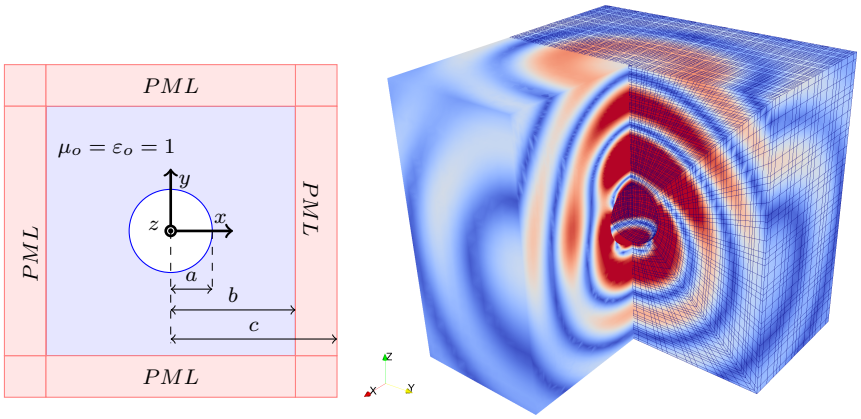

FIG. 8.12. *Spherical obstacle scattering example: 8.12(a) Truncated domain with PML, 8.12(b) Magnitude of the initial scattered magnetic field, $\|\boldsymbol{H}\|$, plotted on a part of a non-conforming curved mesh with solution order of $N = 4$. Also shown are the LGL points on a portion of the mesh.*

where $\hat{H}_n^{(1)}$ denotes spherical Hankel functions of the first kind, and the following relations hold,

$$\beta = \omega, \quad a_n = j^n \frac{2n+1}{n(n+1)} \frac{\hat{J}_n(\beta a)}{\hat{H}_n^{(1)}(\beta a)}, \quad b_n = j^n \frac{2n+1}{n(n+1)} \frac{\hat{J}_n'(\beta a)}{\hat{H}_n^{(1)\prime}(\beta a)}.$$

For our numerical results, the parameters are chosen as follows,

$$\omega = 5, \quad a = 0.25\sqrt{3}, \quad b = 2, \quad c = 3.$$

Since the exact solutions involve infinite series, we simply truncate them using the first 20 terms for computer implementation.

We now numerically study the convergence rate both in h and in N. Figure 8.13(a) shows the L^2-norm error, at $t = 1$ versus the mesh size h for various solution orders N. Figure 8.13(b) plots the L^2-norm error as a function of the solution order N with various mesh sizes h. For this example, it can be observed that we still have exponential convergence behavior in N, but the rate in h is less than $N + 1$ even though it is still better than the DG sharp estimate of $N + 1/2$.

9. Conclusions. We have presented an analysis for a non-conforming *hp*-Discontinuous spectral element method for acoustic wave, elastic wave, elastic-acoustic coupling wave and electromagnetic waves in time domain. We have proved consistency, stability, and convergence under the usual assumption, i.e., affine meshes. Our analytical results hold for both exact numerical integration using tensor product Legendre-Gauss quadratures and inexact numerical integration using tensor product Legendre-Gauss-Lobatto quadratures. We have developed a discrete mortar-based approach to treat non-conforming approximations that does not affect the convergence rates. That is, the convergence rates for conforming approximations remain unchanged as if the approximations were conforming. On each element, we have showed that the h-convergence rate is suboptimal by $1/2$ and N-convergence rate by 1 compared to discontinuous Galerkin literature. We then apply our *hp*-DGSEM method to various problems with different characteristics and physics. The numerical results show that

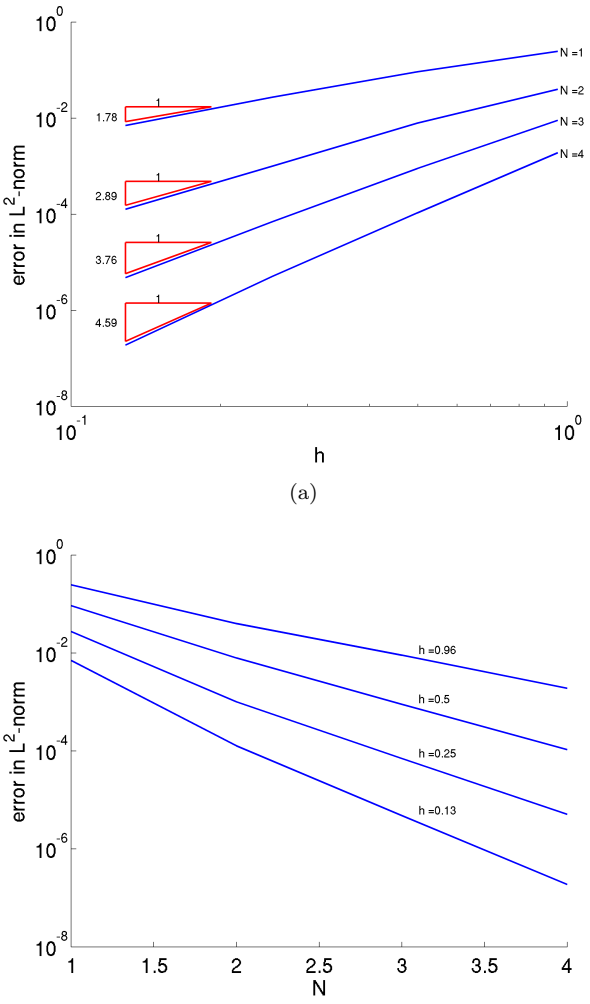

FIG. 8.13. *Spherical obstacle scattering example: 8.13(a) Plot of the error in L^2-norm, i.e. $\|\mathfrak{q} - \mathfrak{q}_d\|_{\mathcal{D}^{N_{el},d}}$, at time $t = 0.125$ as the mesh is refined in h with solution order from $N = 1$ to $N = 4$; 8.13(b) Plot of the error in L^2-norm, i.e. $\|\mathfrak{q} - \mathfrak{q}_d\|_{\mathcal{D}^{N_{el},d}}$, at time $t = 0.125$ as the mesh is refined in N. The convergence is shown for four different mesh sizes $h = \{0.96, 0.5, 0.25, 0.13\}$.*

the convergence rates are optimal, at least $N + 1/2$, in h, and, for element-wise analytic exact solutions, exponential in N. By putting the quadrature points exactly on the curved faces, we numerically observe that our DGSEM method converges for non-conforming approximation with curved meshes. In particular, for all examples with non-conforming meshes in this paper, the convergence rates are optimal.

Acknowledgements. We thank Carsten Burstedde, Georg Stadler, and Lucas Wilcox for countless questions on the **mangll** library, and their DGSEM code for elastic–acoustic waves, from which we built our Maxwell DGSEM code. We also thank them for providing the latex template of the Snell's law for elastic–acoustic waves in their paper [33], from which we built our electromagnetic version in Figure 8.1(a),

and the hexahedral mesh used in our spherical cavity example in Figure 8.10(b). Most importantly, we thank them for many fruitful discussions on their paper [33] and their codes that stimulated our work presented in this paper. We thank Prof. David Kopriva of the Florida State University for his encouragements, without which the paper would not have been possible. We thank Prof. Ivo Babuška for helpful discussions on his approximation results (7.1)–(7.2).

REFERENCES

[1] I. Babuska and M. Suri, *The hp-version of the finite element method with quasiuniform meshes*, Mathematical Modeling and Numerical Analysis, 21 (1987), pp. 199–238.

[2] Ivo Babuška and M. Suri, *The optimal convergence rate of the p-version of the finite element method*, Siam J. Numer. Anal., 24 (1987), pp. 750–776.

[3] I. Babuška and M. Suri, *The p and h−p version of the finite element method, basic principles and properties*, SIAM Review, 36 (1994), pp. 578–632.

[4] Constantine A. Balanis, *Advanced Engineering Electromagnetics*, John Wiley & Son, 1989.

[5] C. E. Baumann and J. T. Oden, *A discontinuous hp finite element method for convection–diffusion problems*, Computational Methods in Applied Mechanics and Engineering, (1999). http://www.ticam.utexas.edu/∼carlosb/.

[6] Jean-Pierre Berenger, *Three dimensional perfectly matched layer for the absorption of electromagnetic waves*, Journal Computational Physics, 127 (1996), pp. 363–379.

[7] C. Canuto, M. Y. Hussaini, A. Quarteroni, and T. A. Zhang, *Spectral methods*, Scientific Computation, Springer-Verlag, Berlin, 2006. Fundamentals in single domains.

[8] B. Cockburn, S. Hou, and C.-W. Shu, *TVD Runge–Kutta local projection discontinuous Galerkin finite element method for scalar conservation laws IV: The multidimensional case*, Mathematics of Computation, 54 (1990), pp. 545–581.

[9] B. Cockburn, G. E. Karniadakis, and C.-W. Shu, *Discontinuous Galerkin Methods: Theory, Computation and Applications*, Lecture Notes in Computational Science and Engineering, Vol. 11, Springer Verlag, Berlin, Heidelberg, New York, 2000.

[10] Bernardo Cockburn and Chi-Wang Shu, *The Runge–Kutta discontinuous Galerkin method for conservation laws v*, Journal of Computational Physics, (1998), pp. 199–224.

[11] M. Durufle, P. Grob, and P. Joly, *Influence of gauss and gauss-lobatto quadrature rules on the accuracy of a quadrilateral finite element method in the time domain*, Numerical methods for partial differential equations, 25 (2009), pp. 526–551.

[12] J. S. Hesthaven, S. Gottlieb, and D. Gottlieb, *Spectral Methods for Time-Dependent Problems*, no. 21 in Cambridge Monographs on Applied and Computational Mathematics, Cambridge University Press, January 2007.

[13] J. S. Hesthaven and T. Warburton, *Nodal high-order methods on unstructured grids. I. Time-domain solution of Maxwell's equations*, Journal of Computational Physics, 181 (2002), pp. 186–221.

[14] Jan S. Hesthaven and Tim Warburton, *Nodal Discontinuous Galerkin Methods: Algorithms, Analysis, and Applications*, vol. 54 of Texts in Applied Mathematics, Springer, 2008.

[15] P. Houston, C. Schwab, and E. Süli, *Disontinuous hp–finute element methods for advection–diffusion problems*, SAM Research Report 2000–07, Seminar fúr Angewandte Mathematik, ETH Zürich, 2000. appeared as [**?**].

[16] Paul Houston, Christoph Schwab, and Endre Suli, *Stabilized hp-finite element methods for first-order hyperbolic problems*, Siam J. Numer. Anal., 37 (2000), pp. 1618–1643.

[17] John Jossey and Anil N. Hirani, *Equivalence theorems in numerical analysis: intergration, differentiation and interpolation*, submitted, (2010).

[18] David A. Kopriva, *A conservative staggered-grid chebyshev multidomain method for*

compressible flows. ii. a semi-structured method, Journal of Computational Physics, 128 (1996), pp. 475–488.

[19] ———, *Metric identities and the discontinuous spectral element method on curvilinear meshes*, Journal of Scientific Computing, 26 (2006), pp. 301–327.

[20] David A. Kopriva, *Implementing Spectral Methods for Partial Differential Equations*, Springer, 2009.

[21] David A. Kopriva and Gregor Gassner, *On the quadrature and weak form choices in collocation type discontinuous Galerkin spectral element methods*, Journal of Scientific Computing, 44 (2010), pp. 136–155.

[22] David A. Kopriva, Stephen L. Woodruff, and M. Y. Hussaini, *Computation of electromagnetic scattering with a non-conforming discontinuous spectral element method*, International Journal for Numerical Methods in Engineering, 53 (2002), pp. 105–122.

[23] Heinz-Otto Kreiss and Godela Scherer, *Method of lines for hyperbolic differential equations*, Siam J. Numer. Anal., 29 (1992), pp. 640–646.

[24] Peter D. Lax and Robert D. Richtmyer, *Survey of the stability of linear finite difference equations*, Communications on Pure and Applied Mathematics, 9 (1956), pp. 267–293.

[25] Todd E. Peterson, *A note on the convergence of the discontinuous Galerkin method for a scalar hyperbolic equation*, Siam J. Numer. Anal., 28 (1991), pp. 133–140.

[26] W. H. Reed and T. R. Hill, *Triangular mesh methods for the neutron transport equation*, Tech. Report LA-UR-73-479, Los Alamos Scientific Laboratory, 1973.

[27] W. J. Rider and R. B. Lowrie, *The use of classical Lax-Friedrichs Riemann solvers with discontinuous Galerkin methods*, Tech. Report LA-UR-01-1282, Los Alamos National Lab, 2001.

[28] C. Schwab, *P– and hp–finite element methods: theory and applications in solid and fluid mechanics*, Oxford University Press, Oxford, 1998.

[29] Chun-Hao Teng, Bang-Yan Lin, Hung-Chun Chang, Hei-Chen Hsu, Chien-Nan Lin, and Ko-An Feng, *A Legendre pseudospectral penalty scheme for solving time-domain maxwell's equations*, Journal of Scientific Computing, 36 (2008), pp. 351–390.

[30] Eleuterio F. Toro, *Riemann Solvers and Numerical Methods for Fluid Dynamics*, Springer, 1999.

[31] E. Turkel and A. Yefet, *Absorbing pml boundary layers for wave-like equations*, Applied Numerical Mathematics, 27 (1998), pp. 533–557.

[32] Eric W. Weisstein, *Lobatto quadrature*, MathWorld.

[33] Lucas C. Wilcox, Georg Stadler, Carsten Burstedde, and Omar Ghattas, *A high-order discontinuous Galerkin method for wave propagation through coupled elastic-acoustic media*, Journal of Computational Physics, 229 (2010), pp. 9373–9396.